The Astronomical Journal, 132:497–513, 2006 August

VIRGO CLUSTER EARLY-TYPE DWARF GALAXIES WITH THE SLOAN DIGITAL SKY SURVEY. I. ON THE POSSIBLE DISK NATURE OF BRIGHT EARLY-TYPE DWARFS

Thorsten Lisker, Eva K. Grebel, and Bruno Binggeli
Astronomical Institute, Department of Physics and Astronomy, University of Basel, Venusstrasse 7,
CH-4102 Binningen, Switzerland; tlisker@astro.unibas.ch
Received 2006 February 3; accepted 2006 April 9

ABSTRACT

We present a systematic search for disk features in 476 Virgo Cluster early-type dwarf (dE) galaxies. This is the first such study of an almost-complete, statistically significant dE sample, which includes all certain or possible cluster members with $m_B \leq 18$ that are covered by the optical imaging data of the Sloan Digital Sky Survey Data Release 4. Disk features (spiral arms, edge-on disks, or bars) were identified by applying unsharp masks to a combined image from three bands (g, r, and i), as well as by subtracting the axisymmetric light distribution of each galaxy from that image. Fourteen objects are unambiguous identifications of disks, 10 objects show "probable disk" features, and 17 objects show "possible disk" features. The number fraction of these galaxies, for which we introduce the term "dEdi," reaches more than 50% at the bright end of the dE population and decreases to less than 5% for magnitudes $m_B > 16$. Although part of this observed decline might be due to the lower signal-to-noise ratio at fainter magnitudes, we show that it cannot be caused solely by the limitations of our detection method. The luminosity function of our full dE sample can be explained by a superposition of dEdis and ordinary dEs, strongly suggesting that dEdis are a distinct type of galaxy. This is supported by the projected spatial distribution: dEdis show basically no clustering and roughly follow the spatial distribution of spirals and irregulars, whereas ordinary dEs are distributed similarly to the strongly clustered E/S0 galaxies. While the flattening distribution of ordinary dEs is typical for spheroidal objects, the distribution of dEdis is significantly different and agrees with their being flat oblate objects. We therefore conclude that the dEdis are not spheroidal galaxies that just have an embedded disk component but are instead a population of genuine disk galaxies. Several dEdis display well-defined spiral arms with grand-design features that clearly differ from the flocculent, open arms typical for late-type spirals that have frequently been proposed as progenitors of dEs. This raises the question of what process is able to create such spiral arms—with pitch angles like those of Sab/Sb galaxies—in bulgeless dwarf galaxies.

Key words: galaxies: clusters: individual (Virgo) — galaxies: dwarf — galaxies: fundamental parameters — galaxies: spiral — galaxies: structure — techniques: image processing

1. INTRODUCTION

At first glance, early-type dwarf galaxies (dEs) are characterized by their smooth appearance, having no recent or ongoing star formation and apparently no gas or dust content. Since they are the most numerous type of galaxy in clusters, it is self-evident that most of the proposed formation scenarios for dEs reflect the vigorous gravitational forces acting within the very environment in which these galaxies typically reside. Ram pressure stripping (Gunn & Gott 1972), galaxy harassment (Moore et al. 1996), and tidal stirring (Mayer et al. 2001) are all based on the removal of gas and the morphological transformation of a late-type spiral or irregular galaxy, thereby attempting to reproduce the seemingly plain appearance of dEs. On the other hand, differences in the chemical abundances of early-type and late-type galaxies may argue against a simple morphological transformation (Grebel et al. 2003). In any case, such structural transformations would be well-suited to explain the famous morphology-density relation (Dressler 1980): the higher the density, the more efficiently are infalling spirals and irregulars transformed into dEs, thereby skewing the relative abundance of different types of galaxy toward massive early-type objects as compared to abundances in the field. Moreover, Conselice et al. (2001) point out that the number of Virgo Cluster dEs is more than a factor of 3 larger than what would be expected from just adding groups to the cluster. This strongly favors the idea that the majority of dEs were formed through a morphological transformation of galaxies that fell into the cluster.

Especially in recent years, small or intermediate-sized samples of dEs have been studied in a large variety of ways. Boselli et al. (2005) find the relation of far-UV–near-UV color and luminosity to be opposite for early-type dwarfs and giants. Van Zee et al. (2004a) derive intermediate ages and subsolar to solar metallicities for dEs via optical multiband photometry. Similar values were reported by Geha et al. (2003) from a Lick index analysis of high-resolution spectra. These spectra and similar studies by van Zee et al. (2004b) and Simien & Prugniel (2002) also revealed a significant amount of rotation in some dEs. Finally, Buyle et al. (2005) presented H I 21 cm line observations as a first study of the interstellar medium of a dE outside the Local Group.

However, no formation scenario could yet be clearly confirmed or rejected. This might be due to a very basic piece of the puzzle still lacking: the unambiguous characterization of dE morphology. Following common definition, dEs comprise both dwarf ellipticals and dwarf S0 (dS0) galaxies; we are not considering the fainter dwarf spheroidal galaxies (e.g., Grebel et al. 2003) or the ultracompact dwarfs (e.g., Hilker et al. 1999) here. The morphological appearance and overall profile of a dwarf elliptical are clearly defined. In contrast, dS0 galaxies are loosely defined as objects whose overall appearance is similar to that of a dwarf elliptical but in which a more detailed examination shows nonelliptical properties, such as lens shape or (central) asymmetries. Binggeli & Cameron (1991) argued that most of these characteristics were indicative of a disk nature, and the authors conjectured that "many, if not most, dS0 systems must be disk

galaxies." However, their existence as a separate class of objects has been put in question by several authors (e.g., Ryden et al. 1999), and dS0s have frequently been treated as a subclass of dwarf ellipticals (e.g., Barazza et al. 2003).

The unambiguous discovery of disk substructure (spiral arms and/or bars) in some dwarf ellipticals and dS0s (Jerjen et al. 2000; Barazza et al. 2002; Geha et al. 2003; Graham et al. 2003; De Rijcke et al. 2003) eventually proved the presence of a disk in at least some dEs. At the same time, however, this raised the question of whether these objects are genuine disk galaxies, i.e., of flat oblate shape and without significant stellar spheroid, or whether they are spheroids hosting just a small disk component like the two low-luminosity ellipticals presented by Morelli et al. (2004). On the theoretical side, Mastropietro et al. (2005) showed that a fraction of the progenitor galaxy's disk is able to survive the morphological transformation from galaxy harassment, providing a possible explanation for disks in dEs.

Since up to now, a systematic analysis of a large sample of dEs for the presence of disk features has been lacking, common practice has been to continue using the original classification of the Virgo Cluster catalog (VCC; Binggeli et al. 1985), therefore calling some objects "dwarf elliptical," some "dS0," and some "dwarf elliptical with embedded disk." In order to avoid confusion, we assign the common abbreviation "dE" to early-type dwarfs in general, thereby meaning both dwarf ellipticals and dS0s. We then examine each object for potential disk substructure, and we introduce the term "dEdi" for a dE with disk features.

Clearly, the small sample of dEdis discovered so far can neither serve as a basis for a revised classification nor is it sufficient to feed formation theories with quantitative input concerning the fraction and properties of such objects. A systematic search for disk features in dEs is thus required and is made possible by the Sloan Digital Sky Survey (SDSS) Data Release 4 (DR4; Adelman-McCarthy et al. 2006), which covers almost the whole Virgo Cluster with multiband optical imaging. With these data at hand, our study can properly address the following questions: (1) whether all objects listed as dS0 in the VCC indeed show disk features, (2) how large the fraction of galaxies with disk features is among dEs, (3) how this fraction is distributed with respect to luminosity, (4) where in the cluster these objects are located, and (5) whether they appear to be genuine disk galaxies or just spheroids with a disk component. The catalog of dEdis and dEdi candidates resulting from this study will serve as important input for all future work on dEs, since the observables under study (e.g., dE colors) can then be correlated with the presence or absence of a disk.

Recently, Aguerri et al. (2005) have introduced a two-component definition of a dS0 based on one-dimensional profile fits, with those (Coma Cluster) objects being called dS0s in which a single Sérsic fit did not lead to a satisfying result and instead a combined Sérsic plus exponential fit was necessary. Our goal in this paper, in contrast, is to uncover disk features on the two-dimensional image without any presumption on one-dimensional profile shapes. To investigate whether the two definitions go hand in hand is beyond the scope of this paper, since it requires that accurate profile fits be done for all our SDSS galaxies. This will be the subject of a future paper in this series.

Our data and sample selection are described in § 2, followed by an outline of the techniques for image analysis in § 3. Identifications of disk features are presented in § 4. Section 5 focuses on the quantitative measurement of spiral features. The flattening distributions of the disk features and galaxies are analyzed in § 6. The luminosity function and number fraction of dEs with and without disk features is the subject of § 7, and the limitations in detecting disk features are considered in § 8. In § 9 we show how our objects are spatially distributed within the Virgo Cluster, and a discussion and summary is given in § 10.

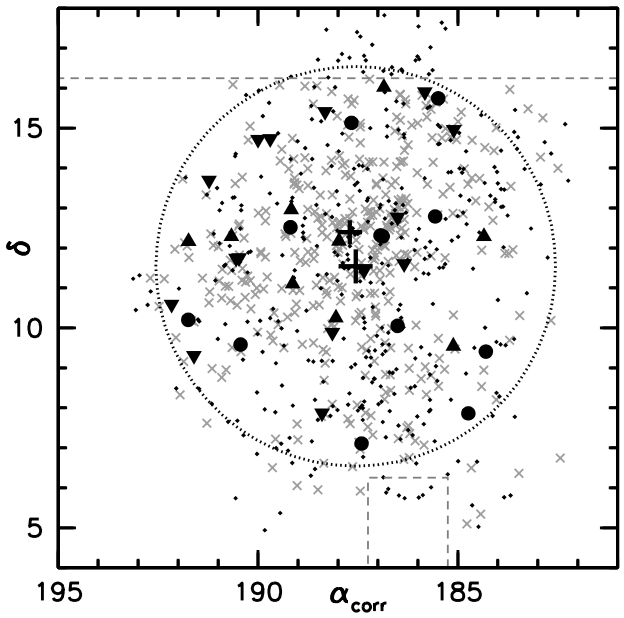

FIG. 1.—Distribution of dEdis within the cluster. Coordinates are given for J2000.0, and right ascension is corrected for the factor cos (δ); see text. Black circles represent unambiguous dEdis, black upward-pointing triangles represent probable dEdis, and black downward-pointing triangles represent possible dEdis. Gray crosses represent dEs in which no disk was found. All other Virgo Cluster galaxies with $m_B \leq 18.0$ mag are shown as small black dots. Only certain cluster members are considered. The upper black cross gives the position of M87, and the lower black cross marks our cluster center, chosen such that the radius of a circle enclosing all dEdis (*dotted black line*) is minimized ($r = 5.^\circ0$). Boundaries of the SDSS coverage are shown as gray dashed lines.

2. DATA AND SAMPLE SELECTION

2.1. *SDSS Images*

The SDSS DR4 covers all galaxies listed in the VCC (Binggeli et al. 1985) with a declination of $\delta \lesssim 16.^\circ25$, except for an approximately $2^\circ \times 2.^\circ5$ area at $\alpha \approx 186.^\circ2$, $\delta \approx +5.^\circ0$ (see Fig. 1). It provides reduced and calibrated images taken in the *u*, *g*, *r*, *i*, and *z* bands with a pixel scale of 0.″396, which corresponds to a physical size of 30 pc when adopting $m - M = 31.0$ mag, i.e., $d = 15.85$ Mpc. The SDSS imaging camera takes data in drift-scanning mode nearly simultaneously in five photometric bands, *u*, *g*, *r*, *i*, and *z*, and thus combines very homogeneous multicolor photometry with large area coverage, good resolution, and sufficient depth to enable a systematic analysis of dEs. The images have an absolute astrometric accuracy of rms $\leq 0.''1$ per coordinate and a relative accuracy between the *r* band and each of the other bands of less than 0.1 pixels (Pier et al. 2003). They can thus easily be aligned using their astrometric calibration and need not be registered manually. The effective exposure time of 54 s leads for a bright dE ($m_B \approx 14$) to a typical total signal-to-noise ratio (S/N) of about 1000 in the *r* band within an aperture radius of approximately 2 half-light radii. For a faint dE ($m_B \approx 18$) this value is typically about 50. The rms of the noise per pixel corresponds to a surface brightness of approximately 24.2 mag arcsec^{-2} in the *u* band, 24.7 in *g*, 24.4 in *r*, 23.9 in *i*, and 22.4 in *z*.

2.2. *Image Stacking*

In order to reach a higher S/N than that of the individual images, we produced a combined image by co-adding the *g*-, *r*-,

and *i*-band images. The *u*- and *z*-band images were not used, since their S/N is significantly lower and would thus lead to a decrease of the S/N of the combined image. When determining the sky level, proper object masks are required so that pixels containing light from a star or a galaxy are excluded from the sky level calculation and only "sky pixels" (i.e., pixels that contain nothing but sky background) remain unmasked. For this purpose, we applied the Source Extractor software (Bertin & Arnouts 1996) to each object's image and each band to yield a "segmentation image" that marks the pixels of all detected sources by assigning them nonzero values. To ensure proper masking of all objects, we expanded the source areas on the segmentation image by smoothing it with a Gaussian filter using IRAF[1] (Tody 1993). The resulting image serves as an object mask. The sky level was then determined with IRAF *imstat* on the so-masked images, along with the noise level, and was subtracted from the images. The *g*- and *i*-band images were shifted with IRAF *imshift* to match the *r*-band image; shifts were determined from the SDSS astrometry provided for each image (see above). We then applied weights $w_{g,r,i}$ to each image, following Kniazev et al. (2004):

$$w_{g,i} = \frac{S_{g,i}\sigma_r^2}{S_r\sigma_{g,i}^2}, \quad w_r = 1, \tag{1}$$

where $S_{g,r,i}$ is the sky level and $\sigma_{g,r,i}$ is the noise level. The weighted *g*-, *r*-, and *i*-band images were then summed to form the final combined image for each object. The resulting total S/N is about a factor of $\sqrt{3}$ larger than in the *r*-band image.

2.3. *Sample Selection*

From visual inspection of the combined images we chose a magnitude limit of $m_B = 18.0$ mag for our study, with m_B provided by the VCC. This is the same magnitude limit up to which the VCC was found to be complete (Binggeli et al. 1985). Adopting $m - M = 31.0$ mag, it corresponds roughly to a limit in absolute magnitude of $M_B \leq -13.0$ mag. A more thorough examination of our limitations in detecting disk features is presented in § 8. Initially, we selected all 552 cluster member and possible member galaxies with $m_B \leq 18.0$ mag that were classified as dwarf elliptical or dS0 in the VCC, including those with uncertainties. We took into account the revised membership and classification from Binggeli et al. (1993), as well as updated classifications for several objects given by Barazza et al. (2002, 2003), Geha et al. (2003), and Lotz et al. (2004). Twenty-five galaxies are not covered by the SDSS DR4. Twenty-five objects with a classification dE/dIrr were excluded, and all the remaining objects were visually examined and excluded if they appeared to be possible dwarf irregulars due to asymmetric features in their images, which applied to 18 galaxies. Thereby we avoided biasing our sample by the inclusion of potential non-early-type objects (which might be disk galaxies anyway). Three more objects (VCC 0184, VCC 0211, and VCC 1941) were classified as possible cluster members but appear to be probable background spirals because of their small size and their spiral arm structure and were therefore excluded as well. Five more objects (VCC 0615, VCC 0811, VCC 1052, VCC 1776, and VCC 1884) are of such low surface brightness that no examination for potential disk features is possible; these were also excluded. Our final sample comprises 476 dEs, 414 of which are definite members of the Virgo Cluster according to Binggeli et al. (1985, 1993).

3. IMAGE ANALYSIS TECHNIQUES

For bringing to light weak features that are hidden by the dominating and mostly smooth and symmetric overall light distribution, two methods have proven suitable. Unsharp masks are a common technique in detecting and enhancing weak substructure, e.g., nuclear bars or spirals (e.g., Lisker et al. 2006; Erwin 2004). They are produced by first smoothing an image and then dividing the original by the smoothed image, which can easily be performed automatically on a large data set. Another technique is to model the smooth axisymmetric light distribution of a galaxy and subtract it from the original image (e.g., Barazza et al. 2002), with nonaxisymmetric features such as spiral arms remaining. Both methods have been used to identify spiral arms, bars, or edge-on disks in eight Virgo Cluster dEs so far (VCC 0490, VCC 0856, VCC 0940, VCC 1010, VCC 1036, VCC 1422, VCC 1488, and VCC 1695; Jerjen et al. 2000, 2001; Barazza et al. 2002; Geha et al. 2003; Ferrarese et al. 2006). These techniques are described below, along with the derivation of an elliptical aperture for each galaxy, which is required as input for both methods.

From our ongoing analysis of dEs with blue central regions (Paper II of this series; T. Lisker et al. 2006, in preparation) we know that a significant fraction of dEs in which no disk features were detected show obvious color substructure. Since we analyze the combined images from three bands in our search for disks, it could happen that color substructure within the galaxy mimics the presence of a disk feature. To test this, we produced (uncalibrated) color maps by dividing the aligned *g*- and *i*-band images. Any detection of a disk feature with the methods outlined below can then be compared to the corresponding color map and can thus be judged for reliability. To investigate whether there are any dEs in which colors do trace disk substructure requires a quantitative color analysis that will be the subject of a future paper in this series.

3.1. *Elliptical Apertures*

An elliptical aperture for each galaxy was determined by performing ellipse fits with IRAF *ellipse* on the combined image, allowing center, position angle, and ellipticity to vary. One of the outer elliptical isophotes, usually between 1 and 2 half-light radii, was then chosen by eye to best trace the *outer* shape of each galaxy, as exemplified for VCC 1010 in Figure 2 (*top left*). This ellipse was adopted to define the ellipticity and position angle of the galaxy.

3.2. *Unsharp Masks*

We produced a set of unsharp masks for each object by smoothing the combined image with a two-dimensional circular and elliptical Gaussian, one at a time, of various kernel sizes σ. A small value of σ will enhance small structures and weaken large features at the same time, while a large kernel size will enhance large structures over small ones. For each set of unsharp masks we chose values of $\sigma = 2$, 4, 6, 9, 13, 20, and 30 pixels. With $d = 15.85$ Mpc ($m - M = 31.0$ mag) and a subsequent pixel scale of 77 pc arcsec^{-1} (30 pc pixel^{-1}), these values correspond to 0.06, 0.12, 0.18, 0.27, 0.40, 0.61, and 0.91 kpc, respectively.

It is desirable to produce both masks created with a circular Gaussian ("circular masks") and masks with an elliptical Gaussian ("elliptical masks") corresponding to the galaxy's ellipticity and position angle. Circular masks of noncircular artificial galaxies show a characteristic narrow shape along the major axis that could

[1] IRAF is distributed by the National Optical Astronomy Observatory, which is operated by the Association of Universities for Research in Astronomy, Inc., under cooperative agreement with the National Science Foundation.

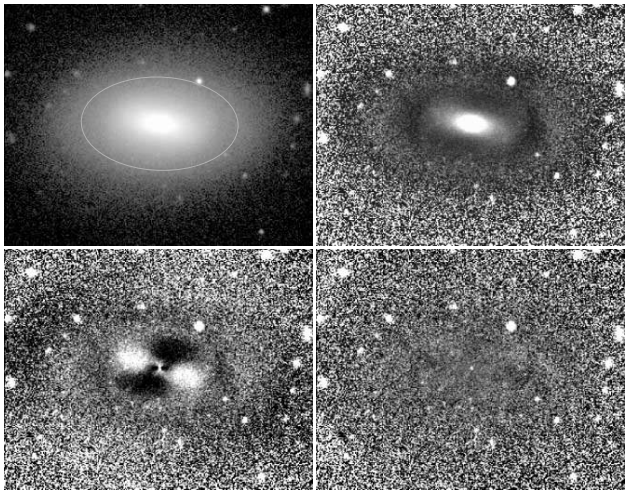

FIG. 2.—Image analysis techniques. *Top left:* Combined image of VCC 1010, along with the elliptical isophote defining its shape. *Top right:* Elliptical unsharp mask with kernel size $\sigma = 20$ pixels. *Bottom left:* Fixed model residual image, i.e., produced via ellipse fits with fixed ellipticity and position angle. *Bottom right:* Variable model residual image, i.e., produced via ellipse fits with variable ellipticity and position angle. Each panel has a horizontal scale of 300 pixels (119″ or 9.13 kpc with $d = 15.85$ Mpc, i.e., $m - M = 31.0$ mag).

easily be confused with an edge-on disk and does not occur when applying elliptical masks. We demonstrate this in Figure 3, where a dE is represented by a two-dimensional exponential surface brightness profile with an elliptical shape (*left*) created with IRAF *mkobjects*. A circular unsharp mask with a Gaussian kernel of $\sigma = 4$ pixels, feigning an edge-on disk, is shown in the middle panel. In the right panel an elliptical mask with position angle and ellipticity matching that of the galaxy has been applied; no substructure is seen. This is due to the fact that the scale radius of the light profile is smaller along the minor axis; therefore, an isotropic Gaussian will blur the object much stronger along the minor than along the major axis. For detection of edge-on disk features or bars that are roughly parallel to the major axis, elliptical masks are thus clearly preferred. However, frequently the inner isophotes of an object are significantly rounder than the outer ones that define the Gaussian's ellipticity. In these cases, an artificial narrow (barlike) structure will again appear along the *minor* axis, due to the very same effect as described above. Here circular masks serve as a complementary check whether an apparent elongated feature along the minor axis is real or is only caused by varying ellipticity.

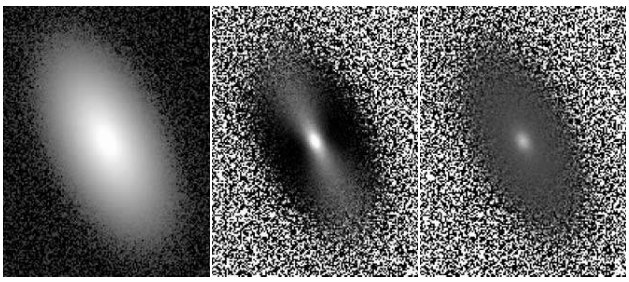

FIG. 3.—Circular and elliptical unsharp masks. *Left:* Simulated galaxy image created with IRAF *mkobjects*, with an exponential intensity profile, a scale length along the major axis of 20 pixels, and an axial ratio of 0.5. *Middle:* Circular unsharp mask of the simulated galaxy, created with a circular Gaussian of kernel size $\sigma = 4$ pixels. An elongated feature appears due to the application of a circular Gaussian to an elliptical object. *Right:* Elliptical unsharp mask with the same kernel size along the major axis, created with an elliptical Gaussian matching the position angle and axial ratio of the galaxy. Each panel has a horizontal scale of 138 pixels.

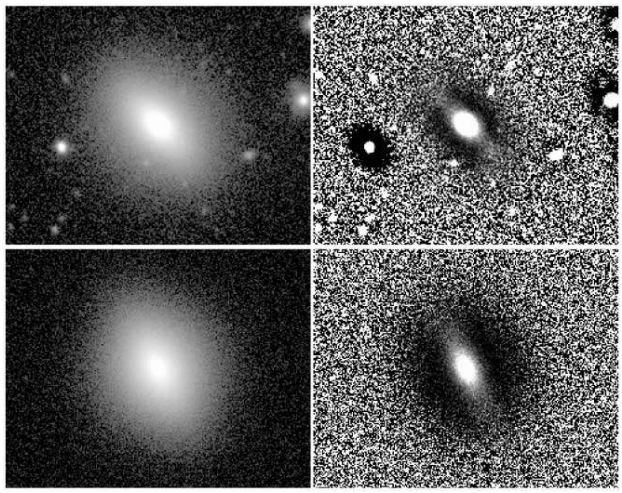

FIG. 4.—Simulated vs. observed dEdi. *Top:* Combined image of VCC 0990 along with its elliptical unsharp mask ($\sigma = 9$ pixels). *Bottom:* Simulated two-component galaxy image along with its elliptical unsharp mask ($\sigma = 9$ pixels). The primary component has an exponential intensity profile with a scale length of 30 pixels and an axial ratio of 1. The secondary component has an exponential intensity profile with equal scale length, an axial ratio of 0.5, and a total magnitude 0.5 mag fainter than that of the primary component. The parameters are chosen to roughly match the appearance of VCC 0990. Note that the simulation contains no nucleus, which is why the central region of the unsharp mask is brighter in the observed image than in the simulated one. Each panel has a horizontal scale of 248 pixels (98″ or 7.55 kpc with $d = 15.85$ Mpc).

3.3. *Residual Images from Ellipse Fits*

A galaxy's surface brightness distribution can be modeled by performing ellipse fits (with IRAF *ellipse*) and then feeding the output directly into the task *bmodel*. The resulting model image is then subtracted from the original object, yielding a residual image. Any information contained in the results of ellipse fitting directly enters the model. This can be nicely demonstrated on VCC 1010, which hosts a bar. If we construct a model through ellipse fits with *variable* position angle and ellipticity, the bar is not seen at all in the residual image (Fig. 2, *bottom right*), since it has been fully reproduced by the model. If position angle and ellipticity are instead fixed at a value taken well outside the bar (namely, the chosen elliptical aperture as described above), a strong residual double cone is seen (Fig. 2, *bottom left*), which has already been explained by Barazza et al. (2002) as the characteristic shape of a changing position angle and therefore of a bar. Similarly, spiral arms can be reproduced to a large extent by varying ellipses and thus do not appear in the residual image unless position angle and ellipticity are kept fixed.

From the above considerations it is obvious that any disk feature can best be detected with a model built through fixed ellipticity and position angle ("fixed model"). However, in principle, any *additional* weak, asymmetric features would require *variable* ellipse parameters ("variable model"), so that the bar or spiral is properly reproduced in the model and fully subtracted from the image, and the additional substructure remains. Therefore, both types of residual images were visually examined along with the unsharp masks for each object.

3.4. *Artificial Galaxies*

In addition to the SDSS data we produced artificial dE galaxies with IRAF *mkobjects*, adopting a two-dimensional exponential surface brightness profile with an elliptical shape (Fig. 3, *left*). This "primary" object was then superposed by another "secondary" exponential light distribution with the same or

higher ellipticity, representing an (inclined) disk within a spheroid (Fig. 4). Various primary-to-secondary flux ratios, scale ratios, position angles, and inclinations were reproduced, in order to provide a model counterpart for real galaxies that potentially are spheroids hosting a disk. The noise characteristics of the artificial images were chosen to be similar to a typical SDSS image, and galaxies covering a range of S/N values were created.

4. RESULTS: EARLY-TYPE DWARFS WITH DISK FEATURES

Close visual inspection of the combined image, the set of unsharp masks, and the two residual images was performed for each galaxy, using the SAOImage DS9 tool (Joye & Mandel 2003). It turned out that unsharp masks are the primary means to search for substructure; especially for small elongated features, they often provide a more reliable and clearer detection than the residual images do. In turn, only in very few cases did the residual images show hints of substructure where the unsharp masks did not. However, in these cases the features were weak and their shape hard to define. Therefore, we adopted a conservative approach and did not consider them as possible substructure. As Barazza et al. (2003) pointed out, care must be taken with features seen solely on the residual images, since the models can be deceived by, e.g., changing ellipticity and position angle, so that the resulting residual image would feign some substructure where none is present. Furthermore, the variable model turned out to be of little use, since it either reproduces substructure completely and yields a blank residual image (see Fig. 2) or leaves only weak features that are readily seen in the unsharp masks and the fixed model residual image. The situation described above, that the variable model would bring to light secondary features by reproducing and subtracting the primary ones, did not occur; i.e., no secondary substructure remained in the residual image other than weak and highly doubtful features.

4.1. *Disk Detections*

We identified 14 out of 476 dEs that unambiguously show disk features, as exemplified in Figure 5 (*top three rows*). Moreover, we find "probable disks" in 10 objects (Fig. 5, *fourth row*) and "possible disks" in 17 objects (Fig. 5, *bottom two rows*). This distinction between unambiguous, probable, and possible disks is based on the visual judgment of all three authors and is intended to be an honest representation of the (un)ambiguity and the S/N of disk features. In the case of a possible edge-on or inclined disk, we used comparisons with artificial two-component galaxies to check whether our interpretation is consistent with such a structure. This is exemplified in Figure 4, where the galaxy VCC 0990—classified as a probable dEdi—is compared to an artificial galaxy consisting of a primary and a secondary component, the latter being fainter and having a larger ellipticity (i.e., representing a larger inclination angle). The simulated image is chosen to be similar in S/N and size, and indeed the shape of the galaxy images, as well as their unsharp masks, look similar.

In two cases (VCC 1684 and VCC 1779) the color maps (see § 3) show a blue central region that is similar in appearance to the possible disk features. As a further test we produced unsharp masks for the two galaxies from the *i*-band images only. However, in both cases we can neither reject nor unambiguously confirm the presence of an inclined disk. We thus list both objects as showing possible disk features.

In several cases we could not decide whether we saw an edge-on disk or a bar; nevertheless, both were taken as disk features, since the presence of a bar commonly requires a disk. Moreover, apart from the simple category "no substructure detected" (applying to 406 objects listed in Appendix E), we labeled 29 galaxies as objects in which substructure of some kind is present but not necessarily indicative of a disk ("other substructure"; objects listed in Appendix E). Seventeen of these show irregular

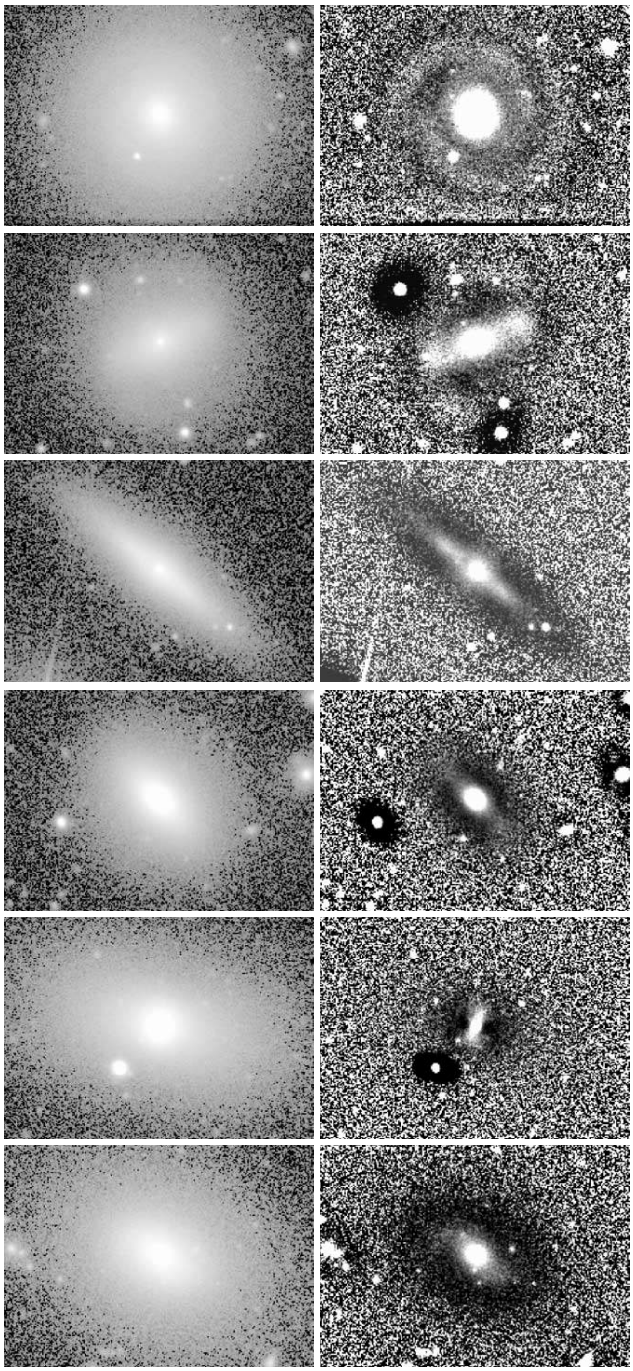

FIG. 5.—Early-type dwarfs with disk features (dEdis). Shown are combined images and unsharp masks for three dEs with unambiguous disk features (*top three rows*), one probable dEdi (*fourth row*), and two possible dEdis (*bottom two rows*). The galaxies are (*top to bottom*) VCC 0308 (spiral arms; unsharp mask kernel size $\sigma = 20$ pixels), VCC 1896 (bar and weak spiral arms; $\sigma = 13$ pixels), VCC 1304 (edge-on disk; $\sigma = 20$ pixels), VCC 0990 (inclined disk, see also Fig. 4; $\sigma = 9$ pixels), VCC 1183 (bar; $\sigma = 6$ pixels), and VCC 2019 (possibly inclined disk, maybe warped or distorted; $\sigma = 13$ pixels). Each panel has a horizontal scale of $98''$ (7.55 kpc with $d = 15.85$ Mpc).

central features (see also § 4.2), five have a boxy shape, four show a feature like a dust lane, and three have unsharp masks that appear to show a luminosity excess in the inner part.

Of the eight Virgo dEs for which disk features have been reported, five (VCC 0490, VCC 0856, VCC 1010, VCC 1036, and VCC 1695) are contained in our 14 unambiguous detections and one (VCC 1422) is a probable detection. Both VCC 0940 (reported by Barazza et al. 2002) and VCC 1488 (reported by Geha et al. 2003) were not even identified as dEdi candidates by us. The reason might be twofold: first, those studies (as well as De Rijcke et al. 2003) used a boxcar or median filter to create their unsharp masks. As we demonstrated above (see Fig. 3 and § 3.2), applying such a filter to a perfectly smooth elliptical light distribution will yield an artificial elongated structure in the unsharp mask. This effect might well apply to VCC 1488 with its axial ratio of 0.55, but less likely to VCC 0940, which has an axial ratio of 0.76. However, the disk features of both galaxies were also reported to be seen in the residual images resulting from ellipse fits and subsequent modeling of the light distribution. Given that both the data from Geha et al. (2003) and from Barazza et al. (2002) are of higher depth and resolution than our SDSS images, the nondetection of ours might simply reflect our limitations in detecting disks and show that more dEdis might exist than those identified by us (see also §§ 7 and 8).

We list the dEdis and dEdi candidates in Table 1. We do not, however, attempt to reclassify objects, since classification schemes in the VCC were fairly complex and based on the surface brightness distribution, whereas we aim solely at stating whether a dE's image shows features of a disk. In principle, it would be desirable to establish a "pure" definition of the dS0 class as those (and only those) dEs hosting (or being) a disk. Unfortunately, this is not possible; apart from the fact that many objects can only be termed candidates due to the limited S/N, those in which no disk was *found* do not necessarily have to *have* no disk. It appears, therefore, most useful to not touch the original VCC classification but instead to provide a list of (candidate) dEdis that can be correlated with all sorts of observables in future studies of dEs. A thorough reclassification of all galaxies is deferred to a future study. We point out that our objects are *not* related to the so-called dwarf spiral galaxies defined by Schombert et al. (1995): while those have a classical bulge, our objects do not.

TABLE 1
Early-Type Dwarfs with Disk Features

VCC	m_B (mag)	$\alpha_{J2000.0}$	$\delta_{J2000.0}$	Membership	Notes
Certain Disks					
1010	13.72	12 27 27.4	+12 17 25	M	3, 4, (5)
0523	13.75	12 22 04.1	+12 47 15	M	3, 4, (5)
2048	13.85	12 47 15.3	+10 12 13	M	1
1036	14.03	12 27 41.2	+12 18 57	M	2
0308	14.30	12 18 50.9	+07 51 43	M	5
0490	14.33	12 21 38.8	+15 44 42	M	5
0856	14.42	12 25 57.9	+10 03 14	M	5
1695	14.60	12 36 54.9	+12 31 12	M	1, 5
1896	14.78	12 41 54.6	+09 35 05	M	3, 5
1671	14.80	12 36 32.2	+06 10 11	P	5
0216	14.90	12 17 01.1	+09 24 27	M	5, (3)
0278	15.10	12 18 14.4	+06 36 14	P	5
1304	15.50	12 30 39.9	+15 07 47	M	2
1204	16.60	12 29 38.0	+07 06 24	M	2
Probable Disks					
1422	13.81	12 32 14.2	+10 15 06	M	1
1949	14.19	12 42 57.8	+12 17 14	M	2, 3, (4)
1947	14.56	12 42 56.4	+03 40 36	P	3, 4
1392	14.62	12 31 55.9	+12 10 28	M	2
0407	14.64	12 20 18.8	+09 32 44	M	2
0990	14.81	12 27 16.9	+16 01 28	M	2
0218	14.88	12 17 05.4	+12 17 22	M	2, (6)
2050	15.20	12 47 20.6	+12 09 59	M	2
0336	16.20	12 19 17.6	+05 52 33	P	1
1691	17.30	12 36 51.1	+12 57 31	M	6, (5)
Possible Disks					
1910	14.17	12 42 08.7	+11 45 15	M	1
1183	14.32	12 29 22.5	+11 26 02	M	3
0389	14.40	12 20 03.3	+14 57 42	M	4
2019	14.55	12 45 20.4	+13 41 34	M	4, (5)
0608	14.70	12 23 01.7	+15 54 20	M	2
2042	14.79	12 46 38.2	+09 18 27	M	4, (5)
1779	14.83	12 39 04.7	+14 43 52	M	2
1684	14.87	12 36 39.4	+11 06 07	M	2, (7)
1836	14.92	12 40 19.6	+14 42 55	M	5
0397	15.00	12 20 12.2	+06 37 24	P	2, 4, (3)
1514	15.10	12 33 37.7	+07 52 17	M	2
1444	15.60	12 32 35.9	+09 53 11	M	6
0788	15.80	12 25 16.8	+11 36 19	M	2
1921	15.90	12 42 26.5	+11 44 25	M	2
2080	16.20	12 48 58.4	+10 35 12	M	2
0854	17.30	12 25 55.7	+12 46 11	M	6
1505	18.00	12 33 24.7	+15 24 28	M	6

Notes.—Objects are sorted by B-band magnitude m_B as given by Binggeli et al. (1985). Cluster membership is provided by Binggeli et al. (1985, 1993): M, certain cluster member; P, possible member. The last column contains information about the nature of the identified features: 1, bar or edge-on disk; 2, inclined disk; 3, bar; 4, disk; 5, spiral arms; 6, too flat for a spheroid; 7, central gas or dust. The latter is an additional feature but is not counted as disk. Numbers in parentheses give uncertain features of which only a hint is present. Units of right ascension are hours, minutes, and seconds, and units of declination are degrees, arcminutes, and arcseconds.

4.2. *Correlation with the Original dS0 Class*

Binggeli & Cameron (1991) described five cases in which a galaxy was classified dS0, with characteristics mostly indicative of a disk nature of the galaxy. Briefly, criteria for dS0s were a bulge-disk-like profile, high flattening, a lenslike appearance, a global asymmetry (like a bar or boxiness), and an irregularity in the central part.

Our initial sample, prior to exclusion of possibly irregular objects, contained 47 out of 50 galaxies classified as dS0 or candidate dS0 (e.g., "dE or dS0") in the VCC. Two objects were then excluded due to a possible irregular nature; thus, 45 (candidate) dS0s are left in our working sample. Twenty-two of these are indeed classified by us as dEdis or dEdi candidates, constituting 54% of our dEdi sample. Fourteen objects have "other substructure," which reflects the criteria of Binggeli & Cameron (1991): three of them have a boxy shape, and nine show irregular or clumpy central features likely caused by gas and dust. As an example for the latter, we show in Figure 6 the image and unsharp masks of VCC 0781, which looks somewhat similar to the well-known dwarf elliptical NGC 205 in the Local Group. Interestingly, all of these nine objects with central gas/dust features have a blue central region with ongoing star formation or at least very young stars, similar to NGC 205 and to the galaxy presented by Gu et al. (2006). This nicely confirms Binggeli & Cameron's conclusion: "the irregularity must stem from recent or ongoing star formation" (drawn without color information or unsharp masks!). None of these galaxies shows (additional) disk features; thus,

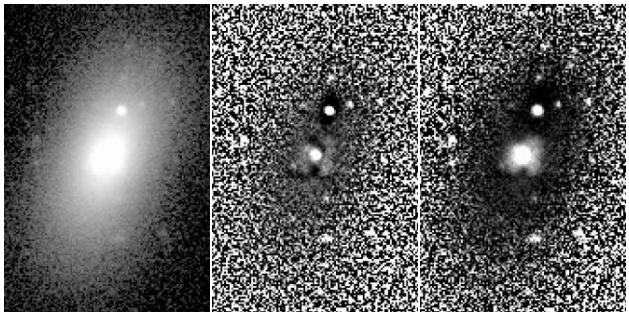

FIG. 6.—A dE with irregular central substructure. Shown is a combined image of VCC 0781 (*left*), an unsharp-mask image with kernel size $\sigma = 4$ pixels (*middle*), and an unsharp mask with $\sigma = 9$ pixels (*right*). Of those dEs in which substructure other than disk features was found, this galaxy represents the subgroup of objects with central irregularities likely to be caused by gas and/or dust. Each panel has a horizontal scale of 46″ (3.53 kpc with $d = 15.85$ Mpc).

caution must be taken when treating them as dEdis only because of their dS0 class: not all classified dS0s are dEdis. These objects might prove highly important for investigating possible formation channels for dEs; therefore, they will be the subject of Paper II of this series (T. Lisker et al. 2006, in preparation).

Finally, for 9 of the 45 (candidate) dS0s, neither a disk nor other substructure was found. However, three of these are classified "dE or dS0," three are "dS0?" (i.e., high uncertainty), and two are "dS0:" (i.e., some uncertainty); hence, we most probably did not miss any significant disk or irregular substructure. The one unambiguously classified dS0 (VCC 1912) had been classified as such mainly due to high flattening. While our measured axial ratio of 0.33 is small, it is not small enough that we would classify it as a dEdi based on flattening only.

5. PROPERTIES OF SPIRAL FEATURES

5.1. *Relative Strength*

For those three dEdis with the best-defined spiral arms, we now attempt to obtain an estimate of the relative amount of light that constitutes the spiral arms, as compared to the smooth and axisymmetrically distributed light. We thus need to measure the flux of the residual image (showing only the spiral arms) within a given aperture and compare it to the total flux of the galaxy within the same aperture. We term this flux ratio the "strength" of the spiral features. However, in the residual image the flux level between the spiral arms is significantly negative. When fitting ellipses, the average flux value of each elliptical isophote is affected by the spiral arms and thus comes out slightly too high. Consequently, somewhat too much flux is assigned to the smoothly distributed light component, resulting in negative flux values when subtracted from the original image. To avoid or at least minimize this effect, we obtain optimized residual images through an iterative procedure outlined in detail in Appendix A, yielding a lower and an upper limit for the strength of the residual features.

The resulting residual images for our three dEdis are presented in Figure 7. Note that it is *not* the case that our disk detections would have been more efficient if we had used such optimized residual images from the beginning. The *contrast* of residual features such as spiral arms does not differ with respect to the initial residual images; only the average flux level is offset systematically.

Apertures enclosing the spiral arms were now chosen manually, and the strength of the spirals was measured from the residual and the model flux within the same aperture. The nucleus, as well as foreground stars or background objects, was masked to avoid any bias. The results are listed in Table 2. VCC 0490 has the strongest spiral features, which amount to 11%–12% of the total light. The spiral of VCC 0308 constitutes 8%–10% of the light, and VCC 0856 only reaches 6%–7%.

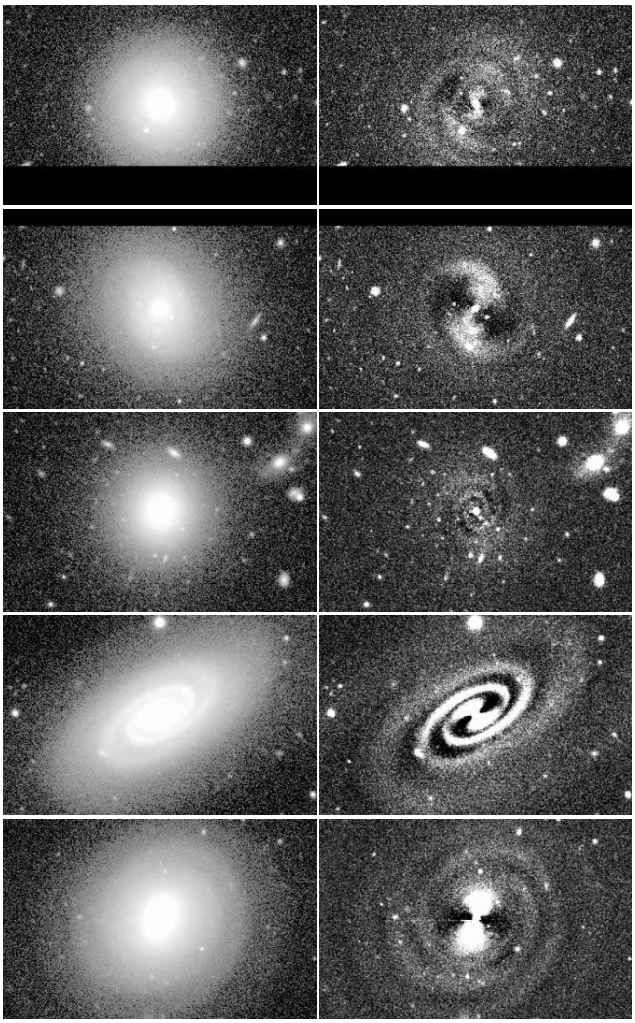

FIG. 7.—Residual images of spiral arms. Combined images, as well as optimized residual images as described in Appendix A, are shown for the three dEdis with the best-defined spiral structure (VCC 0308, VCC 0490, and VCC 0856; *top three rows*), as well as for the two dwarflike S0/Sa galaxies (§ 5.2) VCC 0522 and VCC 1902 (*bottom two rows*). Each panel has a horizontal scale of 162″ (12.48 kpc with $d = 15.85$ Mpc).

With these results at hand, we can now for the first time in the course of this paper address the question of whether dEdis are disk galaxies, i.e., are of flat oblate shape like VCC 1304 (Fig. 5, *third row*), or whether they are spheroids hosting a disk component. The ratio of the light within the spiral features to the smoothly distributed light has been measured to be within 6%–12% for our three galaxies. Therefore, when assuming that these objects are spheroidal galaxies hosting an embedded disk, the total light within the disk cannot be much larger than the light within the spiral features, since otherwise the disk would be the dominating component and the object would not be a spheroidal galaxy in the common sense. Therefore, assuming the light within the spiral features to be of the same order as the total light of the disk component, the above ratio of "spiral light" to the smoothly distributed light should be comparable to the ratio of the secondary to the primary component in our two-component model

TABLE 2
Relative Strength of Spirals

VCC (1)	f_{res}/f_{mod} (2)	Δm (3)	f_{res}/f_{total} (4)	$(f_{res}/f_{mod})_{smooth}$ (5)	Δm_{smooth} (6)	$(f_{res}/f_{total})_{smooth}$ (7)
0308	0.107	2.43	0.097	0.082	2.71	0.076
0490	0.132	2.20	0.117	0.122	2.29	0.108
0856	0.075	2.81	0.070	0.059	3.07	0.056
0522	0.159	2.00	0.137	0.127	2.24	0.113
1902	0.150	2.06	0.131	0.102	2.47	0.093

Notes.—Cols. (2)–(4) give measured values for the optimized residual image *without* median smoothing; cols. (5)–(7) give the same quantities for the version *with* smoothing (see text for details). Cols. (2) and (5) give the ratio of the flux of the residual image to the flux of the model image within the chosen aperture. Cols. (3) and (6) give the same as a magnitude difference, and cols. (4) and (7) give the fraction of residual to total light.

images. If, however, our galaxies would be genuine disk galaxies, the spiral features might well contain just a fraction of the total light of the disk. Consequently, if the disk is seen edge-on and compared to a suitable two-component model image, the ratio of its secondary to primary component should be significantly larger than the value measured for the (face-on) spiral features. Indeed, for those dEdis with apparent inclined disks that could not be confused with a bar, the secondary component of the similar-looking model images is only 0.5–1 mag fainter than the primary component, whereas the spirals measured above are 2.2–3.1 mag fainter than the smooth axisymmetric component. Although this is not final proof due to the small number of objects considered, it points toward dEdis *being* disk galaxies, instead of just *having* a disk component. Further arguments supporting this view are presented in § 6.

5.2. *A Possible Connection to Faint S0/Sa Galaxies*

Since the strengths of the three spirals measured above already differ within a factor of 2, it might be interesting to see how the galaxies' images would appear if their spirals were stronger by a certain amount. For this purpose, we simply multiplied the residual images by a certain factor and added them to the model of the smooth component, thereby mimicking a stronger spiral. Strikingly, with only a 0.5–1 mag enhancement, the galaxy does not look like a dwarf elliptical or dS0 anymore but instead like a spiral galaxy, although without a bulge.

It might thus be no coincidence that more than a decade ago, one of us (B. B.) identified a handful of "faint, dwarfish looking S0/Sa" galaxies in the Virgo Cluster (VCC 0522, VCC 1326, VCC 1368, VCC 1757, and VCC 1902) whose appearance is very similar to what has just been described (Fig. 7). These objects differ from normal (i.e., giant) S0/Sa galaxies: their surface brightness profiles are similar to dEs and remain flatter than the flattest possible King profile when going inward; i.e., they apparently have no bulge (B. Binggeli 1991, unpublished). Thus, they are hardly normal S0/Sa galaxies, which typically have a high bulge-to-disk ratio. Instead, they have a central luminosity excess just like the dEs.

One might thus term these objects "dwarflike S0/Sa" galaxies to distinguish them from their giant counterparts. A further investigation of their characteristics and a detailed comparison with dEs will be the subject of a future paper in this series. For our present study, we selected those two with the best-defined spiral structure (VCC 0522, classified Sa, and VCC 1902, classified S0/Sa), in order to measure the spiral strength like we did above and compare it to the dEdis. Their strengths turn out to be slightly larger than the average value of the three dEdis and similar to the strongest dEdi spiral (VCC 0490): 9%–13% for VCC 1902 and 11%–14% for VCC 0522. Both objects are about half a magnitude brighter than the brightest dEdis. It thus appears plausible that the dEdis and these objects belong to the same population of galaxies that extends to magnitudes brighter than those of dEs and differs from the "classical" dwarf ellipticals.

5.3. *Pitch Angle*

In order to confirm our above hypothesis, we measured the pitch angle of the spiral arms of both dEdis and the dwarflike S0/Sa galaxies on the residual images. We used the method described by Ma (2001): a spiral arm is traced by manually selecting a series of image positions that follow the arm. These are then fitted by a logarithmic spiral, taking into account the galaxy's inclination and position angle, which we adopt from our elliptical apertures (in the case of VCC 1896 these values were taken from the axial ratio measurement of the disk). We measured two arms of VCC 0308, VCC 0490, VCC 0856, and VCC 1896, one arm of each of the two possible cluster members VCC 0278 and VCC 1671, and two arms of the two faint S0/Sa galaxies VCC 0522 and VCC 1902. The resulting values are shown in Figure 8 (*black symbols*) and compared to the values for various Hubble types from Ma et al. (1999; *gray symbols*). The dwarflike Sa VCC 0522 falls within the range of values of the dEdis, while the dwarflike S0/Sa VCC 1902 lies slightly below. The dEdis best agree with Hubble type Sab/Sb, while the dwarflike S0/Sa galaxies, if taken together, fall in the range of type Sab. An independent check of our measurements is provided by Jerjen et al. (2000), who find a pitch angle of 12°.1 for VCC 0856. For the two arms, we derive the values 10°.5 and 12°.1, respectively, thus being in good agreement with those VLT data measurements. Our derived pitch angles are incompatible with spirals of very late type (>Sc), which are often considered as potential progenitors for dEs; see § 10 for a discussion.

6. FLATTENING DISTRIBUTION

A flattening distribution for our galaxies can be obtained in two ways: for the disk features themselves by directly measuring or estimating their axial ratio, and for the galaxies as a whole based on their ellipticities. The first distribution, which we term the "flattening distribution of the disks," serves as a basic test that the features we see are indeed disk features. This is of particular importance for the inclusion of probable and possible disk features in our working sample of dEdis. In order to have a statistically significant sample, e.g., to derive the luminosity function (§ 7), we would like to include not only those dEs with unambiguous disk features but also those with probable and possible disk features into our dEdi working sample. This requires the flattening distribution of disk features to be consistent with the assumption of an intrinsic flat oblate (and circular) shape, which is examined in § 6.1.

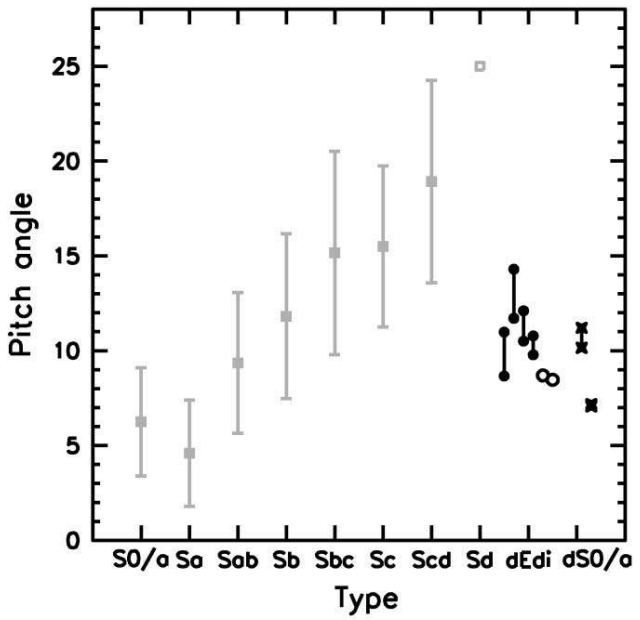

FIG. 8.—Pitch angle vs. morphology. *Gray symbols*: Mean pitch angle and 1 σ error bars of the spiral arms for various Hubble types as given by Ma et al. (1999). The value for type Sd was only derived from two objects. *Black filled circles*: Pitch angle for the certain cluster members VCC 0308, VCC 0490, VCC 0856, and VCC 1896 (*left to right*) for two spiral arms each (*connected symbol pairs*). *Black open circles*: Pitch angle for the possible cluster members VCC 0278 (*left*) and VCC 1671 for one spiral arm each; in both cases the other arm could not be traced well enough. *Asterisks*: Pitch angle for the dwarflike S0/Sa galaxies (see text for details) VCC 0522 and VCC 1902 for two spiral arms each (*connected symbol pairs*; the values for the arms of VCC 1902 are almost equal).

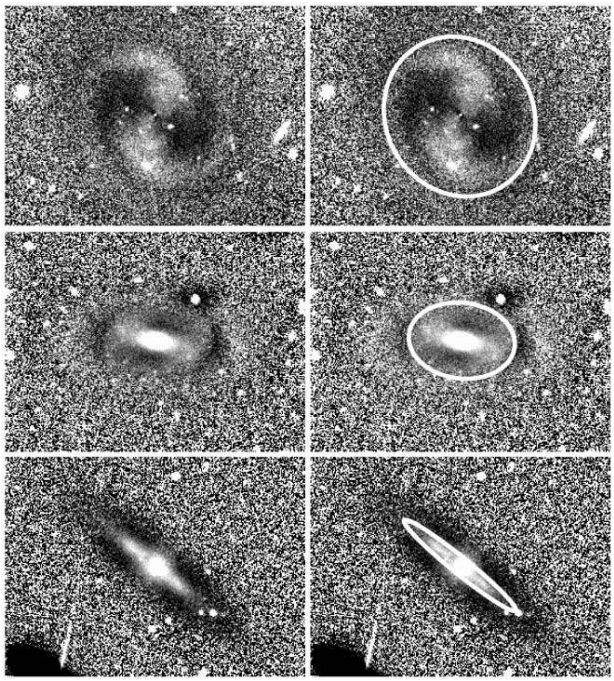

FIG. 9.—Disk axial ratio measurement. The figure illustrates the manual choice of a best-fitting elliptical aperture (*right*) for each disk feature. *Top to bottom:* VCC 0490 (residual image), VCC 1010 (unsharp mask with kernel size $\sigma = 13$ pixels), and VCC 1304 (unsharp mask with $\sigma = 20$ pixels). Each panel has a horizontal scale of 116″ (8.95 kpc with $d = 15.85$ Mpc).

The flattening distribution of the *galaxies*, presented in § 6.2, serves a different purpose: it allows us to consider the question of the possible disk nature of the dEdis again. If they were spheroidal galaxies with a (weak) disk component, the distribution of axial ratios should be significantly different from that of disk galaxies. In turn, if their flattening distribution were consistent with them having an intrinsic disk shape, they would very likely be genuine disk galaxies.

6.1. *Flattening Distribution of the Disks*

Although not possible with perfect accuracy, still an estimate of the inclinations of the disks (not the galaxies) can be obtained from either the unsharp mask or the residual images. An ellipse was manually (by eye) fitted to the disk using that unsharp mask or residual image in which the respective features stand out most prominently (exemplified in Fig. 9). The results are shown in Figure 10 (*left*) as a running histogram (*black line*); i.e., at each data point we consider the number of objects within the chosen bin width of 0.1 ($\pm$0.05). We take into account all 36 dEdis and candidates that are certain cluster members. Galaxies for which we cannot decide whether we see a bar or an edge-on disk were assigned two values: a lower limit assuming an inclined disk (*solid line*) and an upper limit from the axial ratio of the galaxy as a whole, assuming the feature was a bar (*dashed line*). A theoretical distribution assuming a disk with an intrinsic axial ratio following a narrow Gaussian around a mean value $\mu = 0.25$ with $\sigma = 0.01$ and a randomly distributed inclination is shown (*gray line*) for comparison (Mihalas & Binney 1981). Within the expected uncertainties for our relatively crude measurements, the observed and theoretical curve are nicely consistent with each other. This strongly corroborates the hypothesis that the features we see *are* disks, and, moreover, it supports the approach of including not only the unambiguous but also the candidate objects in our dEdi working sample for the purposes of our analysis. As a further test, we examined the flattening distribution for possible disks only; it turns out to be very similar to the distribution for all dEdis. It therefore seems plausible that most of our possible disk detections actually are disks. Nevertheless, we prefer to keep the term "possible" in order to reflect that uncertainties *are* present in our visual identification of disk features.

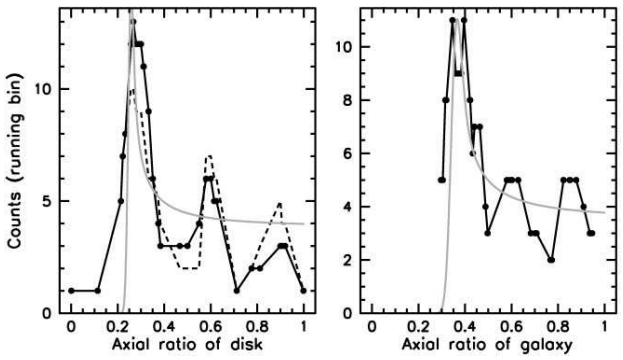

FIG. 10.—Axial ratio distribution for disks and galaxies. The running histogram has a bin width of 0.1 and uses all 36 dEdis with certain cluster membership. *Left:* Distribution of axial ratio measurements of disk features as illustrated in Fig. 9. For the solid black line we assume that all elongated features for which we could not decide between an inclined disk or a bar actually are inclined disks. For the dashed black line we assume that these features are bars and thus adopt the axial ratio of the *galaxy* as an upper limit. The gray line shows the theoretical distribution for an intrinsic axial ratio represented by a narrow Gaussian of $\mu = 0.25$, $\sigma = 0.01$, following Mihalas & Binney (1981). It is normalized to the same area under the curve as the black solid line. *Right:* Distribution of axial ratios of the galaxies. The gray line represents an intrinsic axial ratio that follows a narrow Gaussian of $\mu = 0.35$, $\sigma = 0.02$ and is normalized as above.

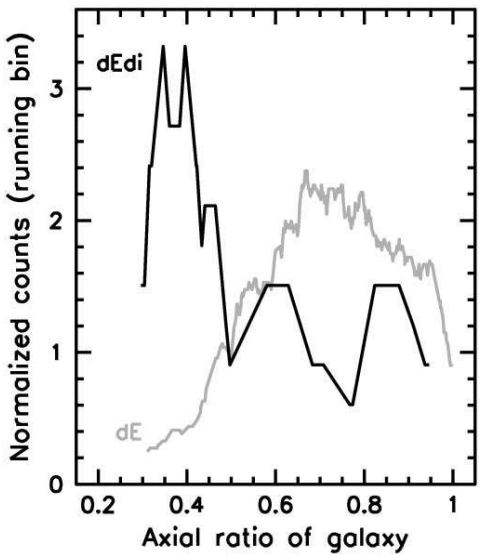

FIG. 11.—Galaxy axial ratio distribution. The running histograms show the galaxy axial ratio distribution of dEdis (*black line*) and dEs in which no disk features were found (*gray line*). Both histograms are normalized to an area of 1.

6.2. *Flattening Distribution of the Galaxies*

Based on the elliptical apertures described in § 3.1 we put together the distribution of axial ratios of the (candidate) dEdis, shown in Figure 10 (*right*) as a running histogram (*black line*). For comparison, we show the theoretical curve assuming an intrinsic axial ratio distribution given by a narrow Gaussian with $\mu = 0.35$ and $\sigma = 0.02$. Obviously, there is almost perfect agreement between observed and theoretical distribution, a compelling indication for an intrinsic disk nature of the dEdis. This view gains further support from the comparison with the distribution of dEs in which no disk features were found (Fig. 11): these objects are clearly consistent with a population of spheroids and differ significantly from the dEdi distribution. It thus appears very likely that dEdis are genuine disk galaxies. A prototypical representation of how these disk galaxies appear when viewed edge-on might be given by VCC 1304 (Fig. 5, *third row*) with its axial ratio of 0.32.

While Binggeli & Popescu (1995) already found dS0s to be significantly flatter than dwarf ellipticals, the difference is even more pronounced for our comparison of dEdis and dEs with no disk detection. This is explained by the fact that not all dS0s are dEdis and vice versa: at least some galaxies that were classified as dS0 might be spheroids (see § 4.2).

The flattening distribution also allows us to test whether *all* bright dEs might actually be dEdis but are not identified as such due to limitations of our detection method. When we modify Figure 11 such that only galaxies of the brightest 1 or 2 mag interval are considered (not shown), the distribution of dEs with no disk detection is inconsistent with all of them being dEdis as well. Therefore, while we might miss *some* dEdis in our search for disk features as outlined in § 8, we can exclude the possibility that *all* of the brightest dEs are disk galaxies; a significant number of objects need to be spheroids.

7. DISK FRACTION VERSUS MAGNITUDE

In Figure 12 (*top*) we show the distribution of dEs and (candidate) dEdis with respect to their *B*-band magnitude provided by the VCC. For this purpose we present our data as a running

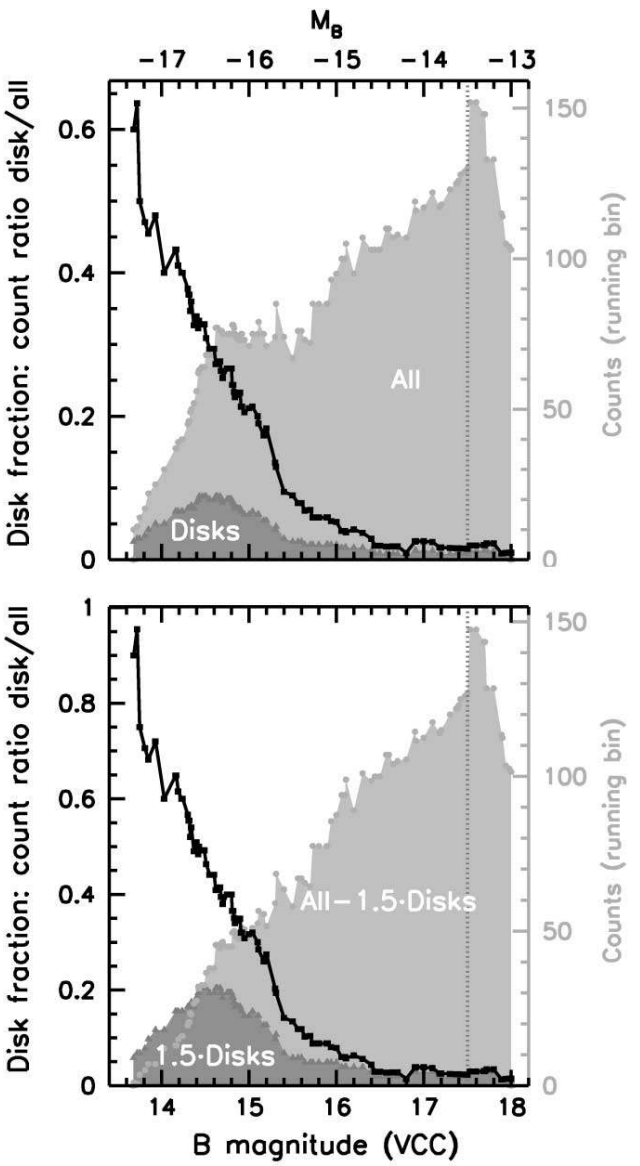

FIG. 12.—Luminosity function and disk fraction. *Top:* Running histogram of the number of all dEs (*light gray*) and (candidate) dEdis (*dark gray*) with respect to *B*-band magnitude as given by the VCC. The bin width is 1.0 mag; therefore, the counts are incomplete for $m_B > 17.5$ mag (*vertical dotted line*). A bin is calculated at each position of a galaxy in the full sample. The upper *x*-axis gives absolute magnitude assuming $m - M = 31.0$ mag. Only certain cluster members are considered. The ratio of both histograms is the disk fraction and is given as a black solid line. *Bottom:* Similar to the top panel, but for all dEs minus 1.5 times the number of (candidate) dEdis (*light gray*), for 1.5 times the number of (candidate) dEdis (*dark gray*), and for the disk fraction resulting therefrom (*black solid line*).

histogram with a bin width of 1.0 mag (i.e., ±0.5 mag). Only galaxies that are certain cluster members according to Binggeli et al. (1985, 1993) are considered, resulting in 414 objects (*light-gray histogram*) containing 36 dEdis and candidates (*dark-gray histogram*). The fraction of (candidate) dEdis among all dEs is shown as a black solid line, which reaches more than 50% for the brightest objects and then decreases to a few percent at $m_B > 16$. This "disk fraction" might be of special interest, since, e.g., Binggeli & Cameron (1991) discuss a potential break in dwarf galaxy structure at $M_{B_T} \simeq -16$, which corresponds to $m_B = 15.7$ given their $m - M = 31.7$.

A plateau is seen in the running histogram (the luminosity function) of our full dE sample, the position of which coincides very well with the location of the dEdis in the diagram. As a test, we subtract the dEdi counts from those of the full sample, but a weak bump remains. However, we need to take into account the fact that we might have missed a significant number of disks in dEs due to the limitations of our data (which are assessed in § 8). Therefore, we now multiply the dEdi counts by 1.5 to account for the missed ones and subtract these counts from those of the full sample. Indeed, the plateau disappears (Fig. 12, *bottom*).

These results, independent of any considerations in previous sections, suggest very convincingly that dEdis are a different population than dEs with no disk; i.e., both have different origins not related to each other. Taken together with the indications for the disk nature of dEdis, evidence accumulates that dEdis are not just dwarf ellipticals with embedded disks but instead constitute a population of disk galaxies different and independent from classical dwarf ellipticals.

In the following we attempt to estimate the number of disks that are missed by our study, in order to assess whether the above assumption of a factor of 1.5 is realistic. Moreover, we attempt to independently show that the decline of the disk fraction is real and cannot be just an effect of limited data quality.

8. LIMITATIONS IN DETECTING DISKS

To obtain a realistic estimate for the limitations in detecting disks, we artificially dimmed our objects such that they correspond to dEs that are fainter by 1 or 2 mag, respectively, also taking into account the relation of dE magnitude and radius (Binggeli & Cameron 1991). This was done on the individual images and is described in more detail in Appendix B. The resulting modified images were then co-added like the original data, and unsharp masks were created. The dimmed objects were then treated as if they were real galaxies that had to be searched for disk features, and the same categories (unambiguous, probable, etc.) were assigned.

In Figure 13 we focus on the galaxies lying within the brightest 1 mag interval (*solid line with filled circles*). When dimmed by 1 mag, they result in the histogram given by the dashed line with crosses, and when dimmed by 2 mag, the resulting histogram is shown by the dot-dashed line with triangles. This illustrates the disk fraction we would *expect* to see at fainter magnitudes *if* the fraction of the brightest 1 mag interval of our sample were constant with magnitude.[2] The obvious mismatch, along with the already strong decrease in disk fraction *within* the brightest 1 mag interval itself, suggests that the observed decline in disk fraction is real and is not due to the limitations of the data. Even if we do not assume the true fraction to be constant, we find down to $m_B \approx 16.0$ mag that the observed disk fraction declines much stronger per 1 mag interval than what would be expected from artificial dimming (see Appendix C).

However, a fair part of the decline *is* still likely to be caused by the latter effect: the curve for objects dimmed by 1 mag lies at about a factor of 1.2 lower than the original one, and the 2 mag curve is even a factor of 2 lower. This shows that our above estimate of the true number of dEdis being larger by 1.5 than what we observe is a useful estimate for the average fraction of missed objects.

Still, the issue might be more subtle; if the *relative strength* of the disk features were decreasing with magnitude in addition to the S/N of the object *as a whole*, the estimate from artificially dimming the galaxies would be somewhat too high. While several of the disk features of the artificially dimmed galaxies would still be strong enough to be seen, some of the true observed ones would not. We examine this possibility in Appendix D and find that indeed somewhat more dEdis than estimated above might be missed at fainter magnitudes due to data limitations. However, if the true disk fraction were to decrease to zero this effect would be of minor relevance. Although we are not able to give an accurate estimate of the true number fraction of dEdis, we point out again that our analysis is consistent with the approximation of multiplying the disk fraction by 1.5 in Figure 12 (*bottom*). A significantly larger factor can be excluded following the argument given in § 6.2: the flattening distribution of the brightest 1 and 2 mag interval of our sample is inconsistent with all bright dEs being disk galaxies and instead requires a significant number of objects to be spheroids.

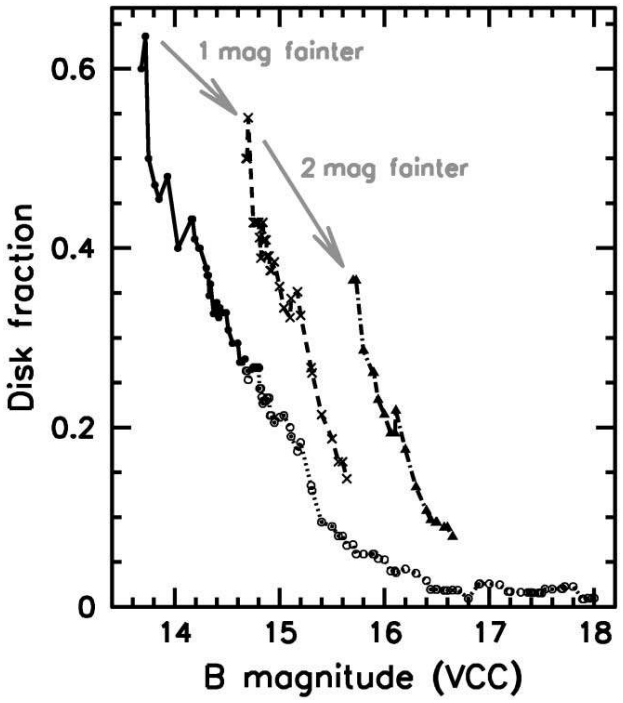

FIG. 13.—Effect of S/N on the disk fraction. A running histogram of the disk fraction, as given in the top panel of Fig. 12 (*solid and dotted lines with circles*), is shown. The brightest 1 mag interval is shown as a solid line with filled circles, changing to a dotted line with open circles outside of the interval. When the dEdis in this interval are dimmed (see text) by 1 mag, the resulting disk fraction is given by the dashed line with crosses. A dimming by 2 mag results in the dot-dashed line with triangles. A histogram bin is calculated at each position of a galaxy in the full sample.

9. SPATIAL DISTRIBUTION

It is well known that the projected spatial distribution of different morphological types of galaxies differs significantly (the so-called morphology-density relation; Dressler 1980). Therefore, it appears interesting to examine the distribution of dEdis and dEs in which no disk was found and compare it to other galaxy types. Those projected spatial distributions are shown in Figure 14, along with, for comparison, the distributions for giant ellipticals (Es), Es and giant S0s together, spiral galaxies, and irregulars. Positions are taken from the VCC by use of the VizieR database (Ochsenbein et al. 2000). Only certain cluster members are considered, and intermediate or uncertain classifications

[2] Here we neglect the fact that there is already a large decrease in disk fraction *within* the brightest 1 mag interval; however, a certain interval width is necessary in order to still have a fair number of dEdis left among the 2 mag dimmed dEs.

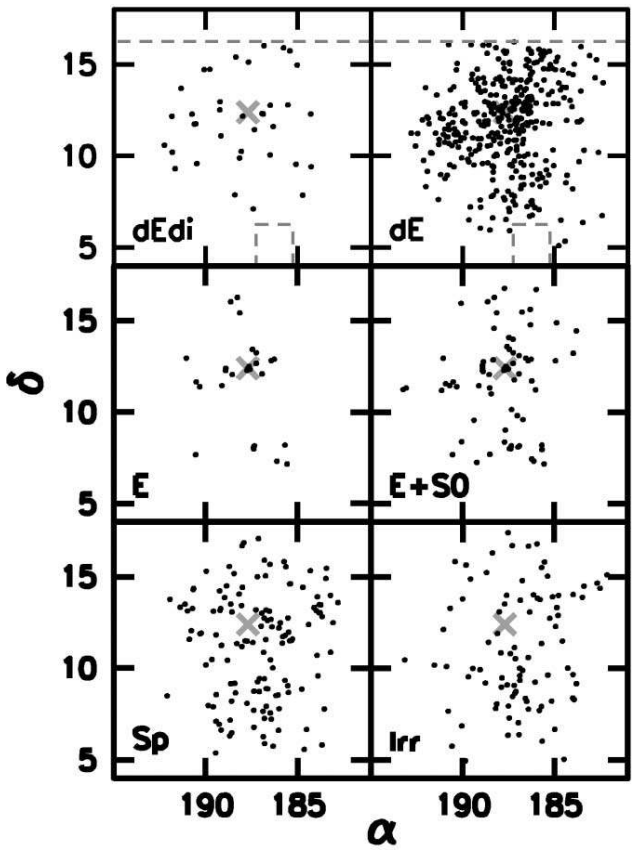

FIG. 14.—Distribution of morphological types within the cluster. For various types of galaxy (dEdis, dEs with no disk features, Es, E+S0s, spirals, and irregulars) the projected spatial distribution is shown. Coordinates are given for J2000.0. Only certain cluster members are considered. The position of M87 is shown as a cross. In the top panels the boundaries of the SDSS coverage are shown as dashed lines.

between the types are excluded.[3] Clearly, dEdis show the least clustering of all types, somewhat similar to the distribution of irregulars with $\delta > 10^{\circ}$.

For a more quantitative analysis, we show the cumulative distribution of each type of galaxy with respect to the distance from the cluster center. Since there is no unique definition for the latter, we decided to choose a point such that the radius of a circle enclosing all dEdis is minimized (Fig. 1). For this purpose we use a "corrected right ascension," which we define as

$$\alpha_{\rm corr} = (\alpha - \alpha_{\rm center}) \cos(\delta) + \alpha_{\rm center}, \qquad (2)$$

so that $\alpha_{\rm corr}$ is measured in true degrees. We choose "our" center to lie at

$$\alpha_{\rm center} = \alpha_{\rm M87} - 0\overset{\circ}{.}15, \quad \delta_{\rm center} = \delta_{\rm M87} - 0\overset{\circ}{.}85, \qquad (3)$$

i.e., going from M87 slightly toward M86 and M49. Interestingly, this circle at the same time encloses exactly all the Es. For all other types, we only consider galaxies up to the maximum radius of the dEdis, in order to properly compare their clustering properties *within* that area. The fact that other galaxy types extend slightly farther outward might have physical significance but could also be just due to the relatively small number of dEdis as compared to other types. Also, a part of it is due to the boundaries of the SDSS DR4 coverage, indicated in the top panels of Figure 14 (*dashed gray lines*).

[3] For example, a galaxy classified as E/S0 is excluded from the sample of Es but included in the combined sample of Es and S0s.

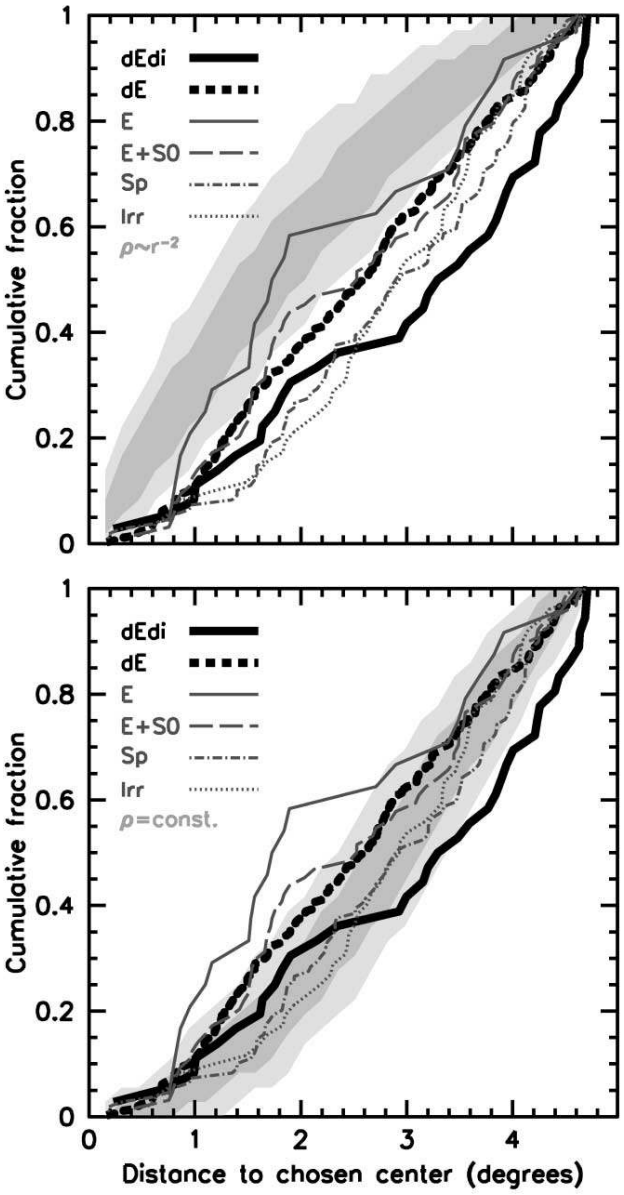

FIG. 15.— Radial distribution of morphological types. Both panels show the cumulative distribution of the angular distances of galaxies from our chosen cluster center (see text). Only certain cluster members are considered, and all galaxy types are only considered up to the maximum distance of the dEdis. Various line types give the cumulative distributions for dEdis, dEs with no disk features, Es, E+S0s, spirals, and irregulars, as labeled in the figure. *Top:* Monte Carlo simulations were performed to yield the expected distribution for an isothermal sphere potential (i.e., $\rho \sim r^{-2}$) for a total number of 36 objects, i.e., the number of (candidate) dEdis. For the simulation, a distance to the Virgo Cluster center of 15.85 Mpc was adopted (corresponding to $m - M = 31$), resulting in an angular scale of 0.28 Mpc deg^{-1}. The simulated objects populate a sphere with a physical radius of 1.4 Mpc, i.e., corresponding to the angular value of $5\overset{\circ}{.}0$ for the circle in Fig. 1. The resulting distribution is shown by gray areas that enclose vertical intervals around the median, containing all but $\pm 15.87\%$ ($\equiv 1\,\sigma$; *dark gray*) and all but $\pm 2.27\%$ ($\equiv 2\,\sigma$; *light gray*) of simulated values. *Bottom:* Analogous Monte Carlo simulations were done for a constant galaxy density. Note that the 1 and 2 σ areas are only valid for a comparison with the dEdis, not with other types, since the number of galaxies is different for the latter.

We show the cumulative distributions in Figure 15. Along with the distribution for different morphological types, we show

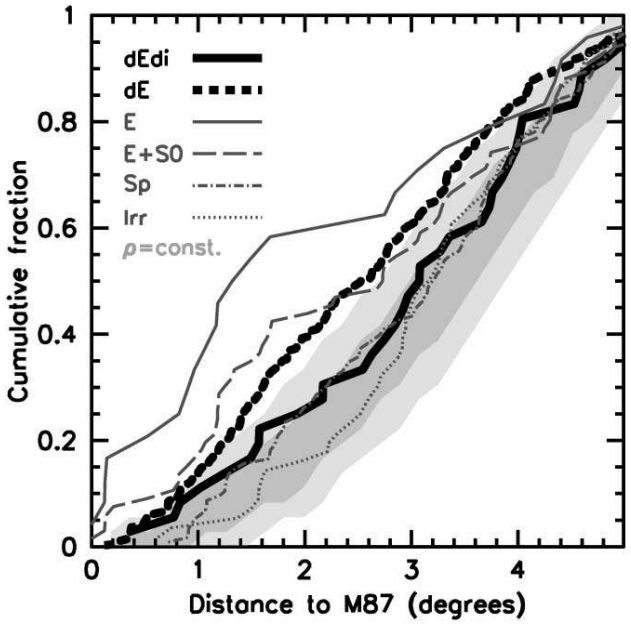

FIG. 16.—Radial distribution with respect to M87. Same as Fig. 15, but now adopting M87 as cluster center.

the expected distribution for an isothermal sphere [$\rho(r) \sim r^{-2}$] in the top panel and for constant density [$\rho(r) = \text{const.}$] in the bottom panel, where $\rho(r)$ denotes the true volume density, not the projected surface density. This is done by populating a (three-dimensional) sphere at the distance of the Virgo Cluster (taken to be $d = 15.85$ Mpc, i.e., $m - M = 31.0$ mag) with the same number of objects as the number of dEdis and then "observing" the projected distribution of this sphere. Vertical intervals containing all but $\pm 15.87\%$ ($\equiv 1\ \sigma$; *dark gray*) and all but $\pm 2.27\%$ ($\equiv 2\ \sigma$; *light gray*) of the Monte-Carlo-simulated values are shown. Although a sphere is clearly not an ideal representation of the dynamically young and unrelaxed Virgo Cluster, this simple model is intended to give at least a rough idea of the actual density distribution of the various galaxy classes.

The well-known difference in the distribution of Es and spirals or irregulars is clearly visible and serves as guidance for the question of what constitutes a *significant* difference between two galaxy types in the diagram. The dEs in which no disks were found roughly follow the distribution of Es and S0s; i.e., they are less centrally clustered than the Es alone but more strongly than spirals and irregulars. In contrast, dEdis clearly lie below this distribution, and for most of the sample they show even less clustering than spirals and irregulars, confirming the impression given by Figure 14. While Es tend toward the isothermal sphere and spirals and irregulars more or less follow the distribution for constant volume density, dEdis lie beyond even the latter—a clear sign of them being not yet virialized and thus being a population that has experienced fairly recent cluster infall.

For the sake of completeness, we also show the resulting distributions when M87 is chosen as the cluster center instead (Fig. 16). The difference between dEdis and dEs is now slightly less pronounced, but it also now varies somewhat less with radius than before. Here the dEdis closely follow the distribution of spirals and fall within the 1 σ area of the theoretical distribution for constant volume density; note, however, that a sphere around M87 is clearly not a good representation of the Virgo Cluster's shape. In contrast to the dEdis, dEs in which no disk features were found approach the distribution of E+S0s and at larger distances reach the distribution of the Es alone.

10. DISCUSSION AND SUMMARY

It is a long-standing question how early-type dwarf galaxies (dEs) form and whether there is more than one formation channel producing them. Current theories include ram pressure stripping, galaxy harassment, or in situ formation. However, for a proper theoretical approach to dE formation, first the characteristics and possible subpopulations of the dE class need to be fully understood and unveiled from the observational side. While the definition of the dS0 class by Binggeli et al. (1985) implied a disk nature of these objects, the fairly diverse classification criteria had to remain suggestive but not compelling for dS0s being disk galaxies. The discovery of disk features in a handful of dEs had not yet been succeeded by a systematic, quantitative study and thus could not provide significant input for models of dE formation.

Moreover, kinematics, which might provide further insight into the presence of disks, are well studied only for a relatively small sample of dEs. With the SDSS data at hand, we performed for the first time a systematic search for disk features in an almost-complete sample of dEs down to $m_B \leq 18.0$ mag and found 41 out of 476 objects showing (possible, probable, or unambiguous) disk features. In light of the diversity of the dEs, one of our primary and most important results is that dEdis most likely constitute a different galaxy population than dEs in which no disk features are found; the bump in the luminosity function of dEs (Fig. 12) is highly unlikely to be an intrinsic characteristic of just a single population, and it is nicely explained by the superposition of dEdis and dEs with no disk features. Therefore, at least two different formation scenarios appear to be required: one each for dEs with and without disk features.

When the first observations of spiral structure in dEs were made, galaxy harassment seemed to provide a simple explanation for the apparently embedded disks in dwarf ellipticals. Mastropietro et al. (2005) showed that the progenitor galaxy's disk need not be completely destroyed during the process of transformation, but part of it is left over inside the newly formed dwarf. However, we point out a main problem with this scenario: how could the observed *well-defined, early-type* spiral arm structure of dEdis be reconciled with them having *late-type* progenitor spirals with their typically flocculent arm structure? Figure 8 directly compares the pitch angle of our objects to that of Scd and Sd galaxies in the diagram and shows an obvious mismatch. If one assumes a relatively weak spiral structure for the late-type progenitor that would quickly disappear after star formation ceases, one might conclude that the above harassment scenario could still be valid, provided that the dEdi spiral structure is purely of tidal origin, as suggested by, e.g., Jerjen et al. (2000). The above question then changes into whether such well-defined spiral arms can be created at all through a process like harassment and what parameters determine their appearance. To confirm that we are not looking at spiral structure traced by regions of star formation, we examined near-infrared *H*-band images for VCC 0308 and VCC 0856 that we obtained through the ESO Space Telescope European Coordinating Facility Science Archive.[4] These images show the very same spiral structure as the optical data, consistent with what would be expected for grand-design, early-type spiral arms. A detailed examination of

[4] Observations made with the ESO New Technology Telescope at the La Silla Observatory under program ID 64.N-0288.

the color properties of the spiral structure will be presented in Paper III of this series (T. Lisker et al. 2006, in preparation).

Even without considering a specific formation theory, our data also allow us to address the question of whether dEdis are genuine disk galaxies or whether they are spheroids hosting a disk. Our distribution of axial ratios for the *disks* (i.e., where we measured the disk features, not the galaxies as a whole) agrees well with the expected distribution assuming an intrinsic axial ratio of 0.25 (Fig. 10, *left*), confirming our general approach to finding disk features in dEs. More importantly, the distribution of axial ratios of the *galaxies* in which disk features were found is also nicely consistent with the assumption of their being disk galaxies with an intrinsic axial ratio of 0.35 (Fig. 10, *right*). This distribution significantly differs from the distribution of dEs with no disk features, the latter being consistent with a distribution of genuine spheroids. We do not see how this could be reconciled with the assumption that dEdis themselves are spheroids; instead, we take these results as a compelling indication of dEdis being disk galaxies, represented by the edge-on view of VCC 1304 (Fig. 5, *third row*).

Could this population of disk galaxies be simply an extension of their giant counterparts? The deduced intrinsic thickness of dEdis (0.35) agrees with the corresponding value for giant Sa galaxies as given by Fouqué et al. (1990) (0.37 for S0/Sa, 0.33 for Sa; Schröder 1995), and the measured pitch angles best agree with Hubble type Sab/Sb (Fig. 8). The dwarflike S0/Sa galaxies presented in § 5.2 could in fact bridge the gap from dEdis to giant disk galaxies. Here the presence or absence of a classical bulge can distinguish between what would be called a giant or a dwarf galaxy. However, dEs are rare in the field environment, while early-type spiral galaxies are preferentially found in the field. This fundamental observation provides evidence against a close relation of dEdis and early-type spirals.

The projected spatial distribution of dEdis within the Virgo Cluster differs significantly from dEs with no disk features and implies that the population of dEdis is not virialized yet. Thus, if dEdis would be the result of a morphological transformation, this should have occurred recently. Any spiral structure of the late-type progenitor galaxies would have had to be destroyed during the process, since the spiral arm characteristics of the dEdis are incompatible with being remainders from Sc/Sd spiral galaxies. While a pure star formation origin of the spiral arms is unlikely (see above), they might originate from the recent galaxy-galaxy interaction that triggered the transformation process. Since such spiral structure would quickly disappear after the interaction ended, one would expect the dEdis to still show structural distortions, i.e., to be less homogeneous in appearance. Moreover, a significant amount of tidal debris should still be present around them. At least the latter issue could be settled observationally with dedicated deep imaging of dEdis and their vicinity.

Even before the discovery of the first spiral structure within a dE by Jerjen et al. (2000), it was obvious from the existence of a dS0 class that treating all dEs as one single population of galaxies always bore the risk of mixing objects that might have had different evolutionary histories. With our systematic search for disk features, we have now provided several strong indications that dEs do indeed consist of two distinct populations of galaxies. Therefore, with our results at hand, we strongly recommend that those objects identified by us as (candidate) dEdis be considered separately from the rest of the dEs in any future study of dEs, e.g., a study of dE colors. Furthermore, one should keep in mind that a significant fraction of the brighter dEs in which we did not *find* any disk features might still *be* dEdis; this possible incompleteness could fake systematic differences between brighter and fainter dEs. We also suggest separately considering objects in which we did not find disk features but that have been classified as dS0 in the VCC, since our results confirm that these also differ from "ordinary" dwarf ellipticals. As a technical recommendation, we advise caution on the interpretation of substructure that is seen in unsharp-mask images created with *isotropic* smoothing of a *noncircular* object: as illustrated in Figure 3, this can lead to artificial elongated features similar to an edge-on disk.

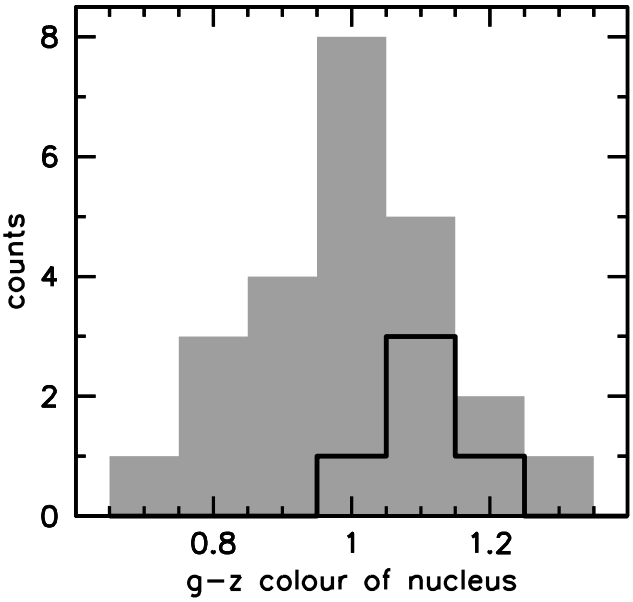

FIG. 17.—Nucleus colors of dEdis. Shown is a histogram of *g-z* colors of dE nuclei (*gray*) as derived by Strader et al. (2005). Five of these objects are dEdis; their nucleus colors are shown by the black histogram.

Now that the separation between dEs and dEdis has been established, their properties can be analyzed. Given the disk nature of the dEdis, a correlation with kinematical studies of dEs is an obvious thing to do. Such a correlation was first investigated by Geha et al. (2003), who found that two out of three rotating dEs show disk features, yet two out of four nonrotating dEs have weak disk substructure as well. Without going into the details of the kinematical analyses, we compiled results from several studies that state whether or not a dE shows significant rotation (van Zee et al. 2004b; Geha et al. 2003; Simien & Prugniel 2002). Note that these studies differ in their data properties, their maximum radius for sampling the rotation curve, and their criteria for significant rotation. Eighteen out of 29 galaxies are found to be not rotationally supported; i.e., they show no or too slow rotation as compared to the observed velocity dispersion. Four of these objects (22%) are (candidate) dEdis. However, it needs to be stressed that rotation curves are only sampled out to about the half-light radius, which might not be enough for definite statements about rotational support. Three of those four dEdis do show significant rotation, but not enough to qualify for being rotationally supported. Of the 11 galaxies that were found to be rotationally supported, 6 (55%) are (candidate) dEdis. There is thus a tendency for dEdis to be rotationally supported systems, as one would expect for disk galaxies. The number statistics are consistent with our rough estimate of one-third of the dEdis being missed in our study when assuming that most or all of them are rotationally supported.

Given the different spatial distribution of dEdis and dEs within the cluster, a further issue of interest would of course be their distribution of heliocentric velocities. These are available for 31

dEdis and 162 dEs in which no disks were found. However, the two distributions do not differ significantly. Since the true three-dimensional locations of our galaxies within the cluster are not known, let alone the exact three-dimensional structure of the cluster itself, unfortunately, no useful conclusion can be drawn here.

To demonstrate how our recommended separation of dEdis and the rest can be applied to other studies of dEs, we show in Figure 17 the colors of dE nuclei derived by Strader et al. (2005): five objects of this sample are identified by us as dEdis and show redder nucleus colors than the bulk of dEs. To obtain a clearer relation, it would be desirable to further pin down the possible disk nature of the remaining dEs in which we could not find disk features. This calls for a larger sample of kinematically studied dEs, as well as for deeper images of higher resolution to detect further substructure, so that more quantitative input for theories of dE and dEdi formation can eventually be provided.

We gratefully acknowledge support by the Swiss National Science Foundation through grant 200020-105260. We thank the referee for constructive suggestions. T. L. would like to thank Victor Debattista for repeatedly affirming that dwarf galaxies *are* interesting. This study would not have been possible without the wealth of publicly available data from the SDSS Data Release 4. Funding for the SDSS has been provided by the Alfred P. Sloan Foundation, the Participating Institutions, the National Aeronautics and Space Administration, the National Science Foundation, the US Department of Energy, the Japanese Monbukagakusho, and the Max Planck Society. The SDSS Web site is http://www.sdss.org. The SDSS is managed by the Astrophysical Research Consortium for the Participating Institutions. The Participating Institutions are the University of Chicago, Fermilab, the Institute for Advanced Study, the Japan Participation Group, The Johns Hopkins University, the Korean Scientist Group, Los Alamos National Laboratory, the Max Planck Institute for Astronomy, the Max Planck Institute for Astrophysics, New Mexico State University, the University of Pittsburgh, the University of Portsmouth, Princeton University, the United States Naval Observatory, and the University of Washington. This research has made use of NASA's Astrophysics Data System Bibliographic Services and the NASA/IPAC Extragalactic Database, which is operated by the Jet Propulsion Laboratory, California Institute of Technology, under contract with the National Aeronautics and Space Administration.

APPENDIX A

RESIDUAL IMAGE OPTIMIZATION

In the residual images obtained in § 3.3, the flux level between the spiral arms is negative. When fitting ellipses, the average flux value of each elliptical isophote is affected by the spiral arms and thus comes out slightly too high (panel *a* of Fig. 18). This results in negative flux values when the model is subtracted from the original image (panel *b*). We construct optimized residual images through the following iterative procedure. Where the initial residual image has negative flux values, its flux is set to zero, otherwise it is left unchanged (panel *c*). The resulting image is then subtracted from the original galaxy image (panel *d*), and a new residual image is obtained as before by fitting ellipses, constructing a new galaxy model, and subtracting it from the original image (panel *e*). This is repeated nine times iteratively, so that the final (tenth) residual image has reached (or come close to) a flux level of zero between the spiral arms (panel *f*). A slight variation of this procedure is to smooth the residual image with a 3×3 pixel median filter each time before the negative flux values are set to zero. It turns out that the final image of the latter version still has a slightly negative overall flux level, while the version without smoothing yields a slightly positive (i.e., too high) overall value in the residual image. We therefore use the strength measurement from the version with smoothing as the lower limit and the one without smoothing as the upper limit.

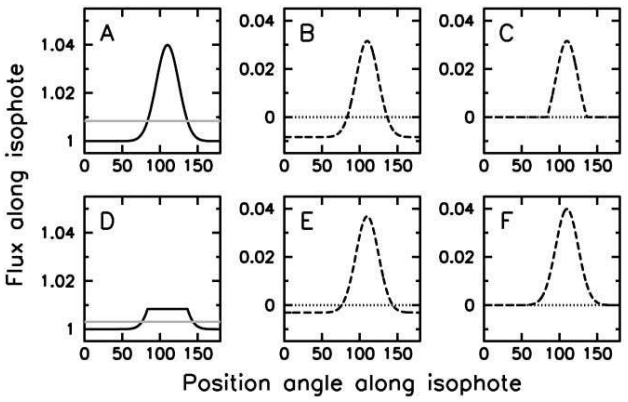

FIG. 18.—Residual image optimization, shown by a sketch of the iterative method for improving the spiral arm residual image. Each panel shows the flux distribution along an elliptical isophote, i.e., with respect to position angle. The isophote is represented by a constant flux value superposed by a crossing spiral arm modeled by a Gaussian. See the text for the details of the method. (*a*) Initial flux shown as a black line, with the average flux value given as a gray line. (*b*) Residual flux shown as a dashed line, with the zero value given as a dotted line. (*c*) Results from (*b*) when all negative values are set to zero. (*d*) Obtained by subtracting (*c*) from (*a*), with the new average flux value given as a gray line. This value is subtracted from the original flux and results in the residual flux given in (*e*). (*f*) Final residual flux after nine iterations.

APPENDIX B

ARTIFICIAL DIMMING OF THE GALAXIES

In order to artificially dim our objects by 1 and 2 mag, first the object size was decreased by a factor of 1.2 per magnitude with IRAF *magnify*, preserving the total flux. This follows the relation of magnitude and radius of the dEs (Binggeli & Cameron 1991): on average, the radius decreases with roughly a factor of 1.2 per magnitude. Since this demagnification also affects the point-spread function (PSF), the image was then convolved with a (normalized) Moffat kernel of proper size so as to approximately reproduce the original SDSS PSF (taken to be 1 FWHM = 4 pixels; Stoughton et al. 2002). We then added noise to the image, with a σ larger by 2.51 or 6.56 compared to the original noise, thereby simulating the S/N of the 1 or 2 mag fainter object. To increase the noise σ by 1 mag, one would actually need to add noise with $\sigma' = (2.51^2 - 1^2)^{1/2}\sigma = 2.30\sigma$. However, since the original noise has already been weakened by demagnifying the image, we chose to use $\sigma' = 2.51\sigma$ as a conservative approximation instead.

APPENDIX C

EFFECT OF S/N ON THE DISK FRACTION

In Figure 19 we show a running histogram of the observed disk fraction (*solid line with filled circles*) and the fraction

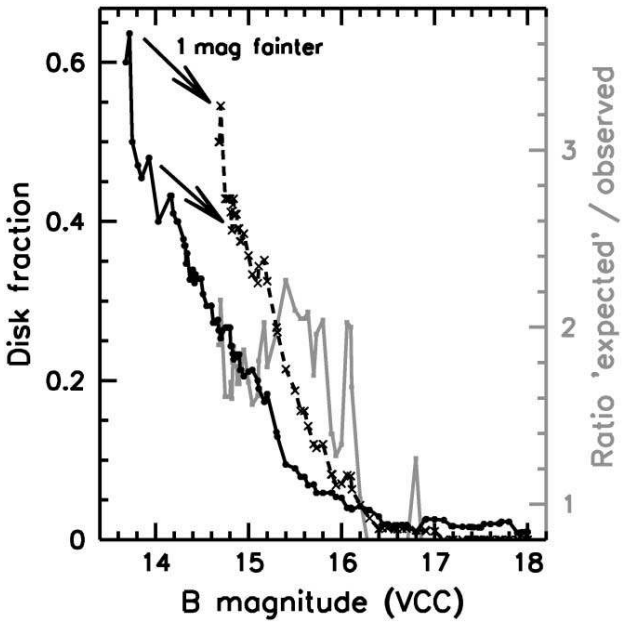

FIG. 19.—Decline of the disk fraction, shown by a running histogram of the disk fraction as given in the top panel of Fig. 12 (*solid line with circles*). When all dEdis are dimmed by 1 mag (see text), the resulting disk fraction is given by the dashed line with crosses. A histogram bin is calculated at each position of a galaxy in the full sample. The gray line gives the ratio of both running histograms and illustrates how much stronger the observed disk fraction declines per 1 mag interval than the expected fraction does from artificial dimming only.

obtained after dimming all objects by 1 mag (*dashed line with crosses*). The original disk fraction lies clearly below the shifted one until the region where both become very small and are affected by small number statistics. It is important to point out that Figure 19 does *not* show how many dEdis would be detected assuming a constant true disk fraction. Instead, since all objects are dimmed by an equal amount (namely, 1 mag), it shows the disk fraction that we would expect to find at a magnitude m when starting from the observed fraction at $m - 1$ and artificially dimming the objects there. Thus, any difference between the observed value at $m - 1$ and the "expected" value at m is due to data limitations only. This is symbolized by the arrows in the figure. Consequently, if the observed decline from $m - 1$ to m is stronger than this expected one, at least part of it has to be real and not only due to data limitations. The ratio between the two curves thus tells us how much stronger the observed decline *per 1 mag interval* is compared to what artificial dimming of the galaxies would predict. We plot this ratio in Figure 19 (*gray line*). Until $m_B \approx 16.0$ mag—where the number of dEdis becomes very small—for each 1 mag step the observed disk fraction declines a factor of 1.5–2.2 stronger than the expected one from limitations of our data only. This clearly shows that the decline of the disk fraction is real.

APPENDIX D

EFFECT OF S/N ON THE FLATTENING DISTRIBUTION OF THE DISKS

Apparent axial ratios of disk features were not only measured on the original images but also on those in which the galaxies had been artificially dimmed, in order to reveal potential changes in the flattening distribution with magnitude. In Figure 20 (*top*) we compare the distribution of disk axial ratios for both the observed

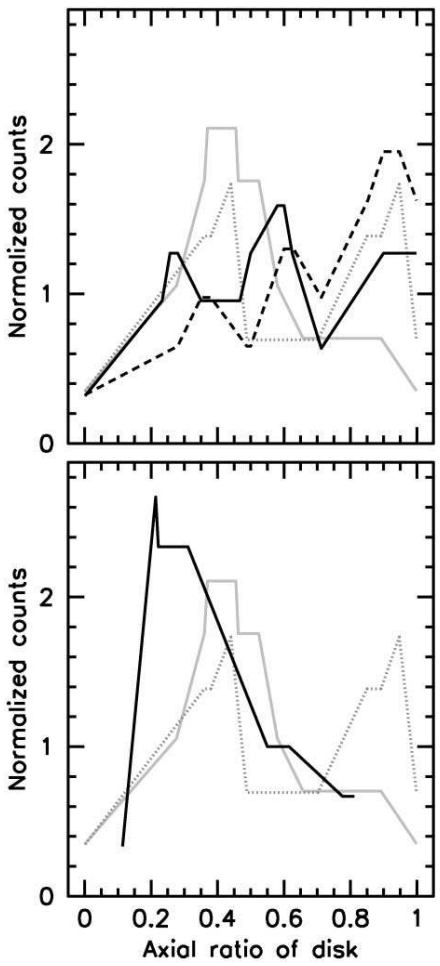

FIG. 20.—Effect of S/N on the flattening distribution. *Top:* Distribution of axial ratio measurements of disk features as illustrated in Fig. 10 (*left*), but this time only for the galaxies in the brightest 1 mag interval. The black lines show the running histogram of the original measurements, while the gray lines give the axial ratios measured for the disk features after artificially dimming the galaxies by 1 mag. The meaning of the solid and dashed lines is analogous to Fig 10; see text for details. A bin is calculated at each data point of each curve with a bin width of 0.2, and the counts are normalized to an area of 1 under the curve. *Bottom:* Same as above, but comparing the observed *second-brightest* 1 mag interval (*black*) to the *brightest* interval dimmed by 1 mag (*gray*; same as top panel).

(*black lines*) and the artificially dimmed (*gray lines*) galaxies that lie within the brightest 1 mag interval of our sample. As in Figure 10, solid lines are derived from lower limits of the axial ratios, dashed lines from upper limits, depending on the interpretation of an elongated feature as a bar or as an edge-on disk. Both curves are normalized to an area of 1. They show a tendency for the dimmed objects toward lower axial ratios, indicating that the (artificial) dimming of objects might slightly prefer disks of certain inclinations over others. However, the distribution of axial ratios for the galaxies of the *observed* second-brightest 1 mag interval is much more clearly skewed toward smaller axial ratios, i.e., larger inclinations (bottom panel of Fig. 20, *black solid line*). While the top panel suggests that part of this is due to the effect of the S/N on the detectability of features such as spiral arms, it might also be that such features are intrinsically weaker, or not even present, in fainter objects. For example, the observed second-brightest 1 mag interval does not contain objects that look like the close-to-face-on spirals in all of VCC 0308, VCC 0490, and VCC 0856, although it does contain galaxies with weaker spiral features that have a larger inclination. Note, however, that the black histogram in the top

panel consists of 16 objects, and both the gray and the black histogram in the bottom panel consist of only 13 objects. Therefore, the axial ratio distributions could at least to some extent be affected by small number statistics. We emphasize that the above effects on the axial ratio of the *disk* features need not go hand in hand with the axial ratios of the *galaxies*. As an example, the weak spiral arms in VCC 1896 are not seen anymore when the galaxy is dimmed by 1 mag. One could then confuse the bar with being an inclined disk and thus measure a much smaller axial ratio of the disk feature, while the galaxy's axial ratio is the same in both cases.

APPENDIX E

OBJECTS IN WHICH NO DISK FEATURES WERE FOUND

VCC numbers of objects in which no substructure was found: 0011, 0029, 0033, 0050, 0061, 0065, 0068, 0070, 0082, 0091, 0096, 0106, 0108, 0109, 0115, 0118, 0127, 0158, 0173, 0178, 0200, 0208, 0227, 0230, 0235, 0236, 0244, 0261, 0273, 0287, 0292, 0294, 0299, 0303, 0317, 0319, 0321, 0330, 0335, 0346, 0361, 0372, 0388, 0390, 0394, 0396, 0401, 0403, 0418, 0421, 0436, 0439, 0440, 0444, 0452, 0454, 0458, 0461, 0466, 0499, 0503, 0504, 0510, 0525, 0539, 0542, 0543, 0545, 0554, 0558, 0560, 0561, 0587, 0592, 0594, 0600, 0611, 0622, 0632, 0634, 0652, 0653, 0668, 0674, 0684, 0687, 0695, 0706, 0711, 0723, 0725, 0745, 0746, 0747, 0748, 0750, 0753, 0755, 0756, 0760, 0761, 0762, 0765, 0769, 0775, 0777, 0779, 0786, 0790, 0791, 0795, 0803, 0808, 0810, 0812, 0815, 0816, 0817, 0820, 0823, 0824, 0833, 0838, 0839, 0840, 0846, 0855, 0861, 0862, 0863, 0871, 0872, 0877, 0878, 0882, 0896, 0916, 0917, 0920, 0926, 0928, 0930, 0931, 0933, 0936, 0940, 0949, 0953, 0965, 0972, 0974, 0976, 0977, 0983, 0991, 0992, 0997, 1005, 1028, 1034, 1039, 1040, 1044, 1059, 1064, 1065, 1069, 1073, 1075, 1076, 1079, 1087, 1089, 1092, 1093, 1099, 1101, 1104, 1105, 1107, 1111, 1115, 1119, 1120, 1122, 1123, 1124, 1129, 1132, 1137, 1149, 1151, 1153, 1163, 1164, 1167, 1172, 1173, 1185, 1191, 1198, 1207, 1209, 1210, 1212, 1213, 1218, 1222, 1223, 1225, 1228, 1235, 1238, 1239, 1240, 1246, 1254, 1261, 1264, 1268, 1296, 1298, 1302, 1307, 1308, 1311, 1314, 1317, 1323, 1333, 1337, 1348, 1351, 1352, 1353, 1355, 1366, 1369, 1373, 1384, 1386, 1389, 1396, 1399, 1400, 1402, 1407, 1414, 1417, 1418, 1420, 1430, 1431, 1432, 1438, 1441, 1443, 1446, 1449, 1451, 1453, 1464, 1472, 1481, 1482, 1488, 1489, 1491, 1495, 1496, 1498, 1503, 1509, 1517, 1518, 1519, 1523, 1528, 1531, 1533, 1539, 1549, 1553, 1561, 1563, 1565, 1571, 1573, 1577, 1599, 1601, 1603, 1604, 1606, 1609, 1616, 1622, 1629, 1642, 1643, 1647, 1649, 1650, 1651, 1652, 1657, 1658, 1661, 1663, 1669, 1674, 1677, 1682, 1683, 1687, 1688, 1689, 1702, 1704, 1710, 1711, 1717, 1719, 1729, 1733, 1740, 1745, 1755, 1761, 1762, 1764, 1767, 1773, 1785, 1792, 1794, 1796, 1803, 1806, 1812, 1815, 1826, 1828, 1829, 1831, 1839, 1843, 1857, 1861, 1866, 1867, 1870, 1876, 1879, 1881, 1886, 1887, 1890, 1891, 1893, 1895, 1897, 1901, 1909, 1912, 1915, 1917, 1919, 1928, 1934, 1936, 1942, 1945, 1948, 1950, 1951, 1958, 1964, 1966, 1967, 1971, 1980, 1982, 1983, 1991, 1995, 2004, 2008, 2011, 2012, 2014, 2017, 2028, 2032, 2043, 2049, 2051, 2054, 2056, 2061, 2063, 2074, 2078, 2081, 2083, and 2088.

VCC numbers of objects in which substructure other than a disk was found (see § 4.1): 0009, 0021, 0046, 0170, 0209, 0281, 0288, 0338, 0501, 0636, 0781, 0870, 0929, 0951, 0962, 1078, 1288, 1334, 1370, 1395, 1457, 1501, 1512, 1567, 1617, 1668, 1715, 1743, and 2045.

REFERENCES

Adelman-McCarthy, J. K., et al. 2006, ApJS, 162, 38
Aguerri, J. A. L., Iglesias-Páramo, J., Vílchez, J. M., Muñoz-Tuñón, C., & Sánchez-Janssen, R. 2005, AJ, 130, 475
Barazza, F. D., Binggeli, B., & Jerjen, H. 2002, A&A, 391, 823
———. 2003, A&A, 407, 121
Bertin, E., & Arnouts, S. 1996, A&AS, 117, 393
Binggeli, B., & Cameron, L. M. 1991, A&A, 252, 27
Binggeli, B., & Popescu, C. C. 1995, A&A, 298, 63
Binggeli, B., Popescu, C. C., & Tammann, G. A. 1993, A&AS, 98, 275
Binggeli, B., Sandage, A., & Tammann, G. A. 1985, AJ, 90, 1681
Boselli, A., et al. 2005, ApJ, 629, L29
Buyle, P., De Rijcke, S., Michielsen, D., Baes, M., & Dejonghe, H. 2005, MNRAS, 360, 853
Conselice, C. J., Gallagher, J. S., & Wyse, R. F. G. 2001, ApJ, 559, 791
De Rijcke, S., Dejonghe, H., Zeilinger, W. W., & Hau, G. K. T. 2003, A&A, 400, 119
Dressler, A. 1980, ApJ, 236, 351
Erwin, P. 2004, A&A, 415, 941
Ferrarese, L., et al. 2006, ApJS, 164, 334
Fouqué, P., Bottinelli, L., Gouguenheim, L., & Paturel, G. 1990, ApJ, 349, 1
Geha, M., Guhathakurta, P., & van der Marel, R. P. 2003, AJ, 126, 1794
Graham, A. W., Jerjen, H., & Guzmán, R. 2003, AJ, 126, 1787
Grebel, E. K., Gallagher, J. S., & Harbeck, D. 2003, AJ, 125, 1926
Gu, Q., Zhao, Y., Shi, L., Peng, Z., & Luo, X. 2006, AJ, 131, 806
Gunn, J. E., & Gott, J. R. I. 1972, ApJ, 176, 1
Hilker, M., Infante, L., Vieira, G., Kissler-Patig, M., & Richtler, T. 1999, A&AS, 134, 75
Jerjen, H., Kalnajs, A., & Binggeli, B. 2000, A&A, 358, 845
———. 2001, in ASP Conf. Ser. 230, Galaxy Disks and Disk Galaxies, ed. J. G. Funes & E. M. Corsini (San Francisco: ASP), 239
Joye, W. A., & Mandel, E. 2003, in ASP Conf. Ser. 295, Astronomical Data Analysis Software and Systems XII, ed. H. E. Payne, R. I. Jedrzejewski, & R. N. Hook (San Francisco: ASP), 489
Kniazev, A. Y., Grebel, E. K., Pustilnik, S. A., Pramskij, A. G., Kniazeva, T. F., Prada, F., & Harbeck, D. 2004, AJ, 127, 704
Lisker, T., Debattista, V. P., Ferreras, I., & Erwin, P. 2006, MNRAS, in press (astro-ph/0509610)
Lotz, J. M., Miller, B. W., & Ferguson, H. C. 2004, ApJ, 613, 262
Ma, J. 2001, Chinese J. Astron. Astrophys., 1, 395
Ma, J., Zhao, J. L., Shu, C. G., & Peng, Q. H. 1999, A&A, 350, 31
Mastropietro, C., Moore, B., Mayer, L., Debattista, V. P., Piffaretti, R., & Stadel, J. 2005, MNRAS, 364, 607
Mayer, L., Governato, F., Colpi, M., Moore, B., Quinn, T., Wadsley, J., Stadel, J., & Lake, G. 2001, ApJ, 559, 754
Mihalas, D., & Binney, J. 1981, Galactic Astronomy: Structure and Kinematics (2nd ed.; San Francisco: Freeman)
Moore, B., Katz, N., Lake, G., Dressler, A., & Oemler, A. 1996, Nature, 379, 613
Morelli, L., et al. 2004, MNRAS, 354, 753
Ochsenbein, F., Bauer, P., & Marcout, J. 2000, A&AS, 143, 23
Pier, J. R., Munn, J. A., Hindsley, R. B., Hennessy, G. S., Kent, S. M., Lupton, R. H., & Ivezić, Ž. 2003, AJ, 125, 1559
Ryden, B. S., Terndrup, D. M., Pogge, R. W., & Lauer, T. R. 1999, ApJ, 517, 650
Schombert, J. M., Pildis, R. A., Eder, J. A., & Oemler, A. J. 1995, AJ, 110, 2067
Schröder, A. 1995, Ph.D. thesis, Univ. Basel
Simien, F., & Prugniel, P. 2002, A&A, 384, 371
Stoughton, C., et al. 2002, AJ, 123, 485
Strader, J., Brodie, J. P., Spitler, L., & Beasley, M. A. 2005, AJ, submitted (astro-ph/0508001)
Tody, D. 1993, in ASP Conf. Ser. 52, Astronomical Data Analysis Software and Systems II, ed. R. J. Hanisch, R. J. V. Brissenden, & J. Barnes (San Francisco: ASP), 173
van Zee, L., Barton, E. J., & Skillman, E. D. 2004a, AJ, 128, 2797
van Zee, L., Skillman, E. D., & Haynes, M. P. 2004b, AJ, 128, 121